JLR RESEARCH ARTICLE

Cadmium-cardiolipin disruption of respirasome assembly and redox balance through mitochondrial membrane rigidification

Nadiya Romanova[1], Kevin Sule[2], Travis Issler[2], Daniel Hebrok[1], Marcus Persicke[3,4], Frank Thévenod[1,5], Elmar J. Prenner[2]*, and Wing-Kee Lee[1]*

[1]Physiology and Pathophysiology of Cells and Membranes, Medical School OWL, Bielefeld University, Bielefeld, Germany; [2]Department of Biological Sciences, University of Calgary, Calgary, Canada; [3]Proteomics and Metabolomics Core Facility, Medical School OWL, and [4]Microbial Genomic and Biotechnology, Center for Biotechnology, Bielefeld University, Bielefeld, Germany; and the [5]Institute of Physiology and Pathophysiology, ZBAF, Witten/Herdecke University, Witten, Germany

Abstract The environmental pollutant cadmium (Cd) poses a threat to human health through the consumption of contaminated foodstuffs culminating in chronic nephrotoxicity. Mitochondrial dysfunction and excessive reactive oxygen species (ROS) are key to Cd cellular toxicity. Cd-lipid interactions have been less considered. We hypothesized Cd binding to the inner mitochondrial membrane (IMM) phospholipid cardiolipin (CL) and membrane rigidification underlies defective electron transfer by disrupted respiratory supercomplexes (SCs). In Cd-treated rat kidney cortex (rKC) mitoplasts, laurdan (lipid-water interface), and diphenylhexatriene (hydrophobic core) revealed increased and decreased membrane fluidity, respectively. Laurdan-loaded pure CL or IMM biomimetic (40 mol % POPC, 35 mol % DOPE, 20 mol % TOCL, 5 mol % SAPI) nanoliposomes were rigidified by 25 μM Cd, which was confirmed in live-cell imaging of laurdan or di-4-ANEPPDHQ loaded human proximal convoluted tubule (HPCT) cells. Blue native gel electrophoresis evidenced ~30% loss of $I+III_2+IV_n$ SC formation after 5 μM Cd for 6 h in HPCTs, which was reversed by CL-binding drug MTP-131/SS-31/elamipretide (0.1 μM), yet α-tocopherol-insensitive. Moreover, MTP-131 attenuated Cd-induced H_2O_2 (~30%) and cytochrome *c* release (~25%), but not osmotic swelling, in rKC mitochondria as well as Cd-induced ROS (~25%) in HPCTs. MTP-131 binding to IMM biomimetic nanoliposomes decreased zeta potential, prevented Cd-induced liposome size increase, and membrane rigidification reported by laurdan. Heterologous *CRLS1* expression reversed Cd (5 μM, 24 h) cytotoxicity (~25%) by MTT assay, Cd (5 μM, 3 h)-induced ROS and mitochondrial membrane rigidification by Cd (1 μM, 1 h) in HPCT cells. In summary, we report a novel mechanism for Cd toxicity in which Cd-CL interactions cause IMM rigidification, thereby disrupting correct SC assembly and increasing ROS.

Supplementary key words heavy metal • toxicity • reactive oxygen species • electron transport chain • liquid-ordered phase

In humans, the kidney is the major site of chronic cadmium (Cd) toxicity, regardless of exposure route. In the renal proximal tubule, filtered unbound and low molecular-weight protein-bound Cd (1), such as metallothionein (MT) (2), a zinc-binding protein, or the antioxidant glutathione (GSH) (3), are internalized by polarized epithelial tubule-lining cells and trapped intracellularly by metal-binding proteins, for example, MT, resulting in biomagnification. As metal-binding capacity becomes exhausted, Cd elicits cellular toxicity and/or cellular stress responses (4, 5), and chronic renal disease (6, 7). Metals interact with cell membranes (8) through which lipid composition, membrane fluidity, and membrane protein function can be altered (9, 10). Indeed, Cd has truly pleiotropic effects and exhibits preferential interaction with some specific amino acid residues (11) and anionic and dianionic lipids (12).

Mitochondria are the main source of reactive oxygen species (ROS), which can cause superoxide anion ($O_2^{\bullet-}$)-dominated physiological oxidative (eu)stress or pathophysiological oxidative distress through accruing levels of hydrogen peroxide (H_2O_2) (13, 14). The electron transport chain (ETC) in the inner mitochondrial membrane (IMM) is comprised of four multimeric complexes (CI-CIV) with donor redox centers for the transfer of electrons, generating energy to create a proton gradient that drives ATP synthesis through the F_1F_0-ATP synthase (15). Inefficient electron transfer at distinct ETC sites causes leakage of electrons and reaction with oxygen, generating ROS. The ETC

*For correspondence: Elmar J. Prenner, eprenner@ucalgary.ca; Wing-Kee Lee, wing-kee.lee@uni-bielefeld.de.

 https://doi.org/10.1016/j.jlr.2025.100750

complexes assemble into respiratory supercomplexes (SCs) of varying stoichiometry of CI, CIII, and CIV. The most abundant is the respirasome (I_n+III_2+IV_n), where most CI is found in SCs with CIII and CIV (16), and the extent of SC assembly dictates the levels and types of ROS generated (17, 18).

Mitochondria are particularly susceptible to Cd effects because of strong Cd accumulation (19), membrane transporters (20), Cd-binding thiol groups (21), and metal-binding sites in the ETC (22) that are targeted by Cd. Uptake of Cd via the mitochondrial calcium uniporter (MCU) (23, 24) elicits (reversible) swelling of the matrix (25, 26), ETC inhibition (27), and release of proapoptotic proteins (28). Furthermore, Cd binds cardiolipin (CL) (12), a mitochondria-specific diphosphatidylglycerol lipid containing four acyl and two phosphate groups with potentially two negative charges each. CL is required for respiratory SC assembly (29, 30) and facilitates negative IMM curvature (31).

Elevated net ROS levels are a hallmark of Cd toxicity (3, 4, 27, 32) that may stem from increased production, e.g. activation of NADPH oxidases or perturbed electron shuttling (27), or from reduced antioxidative capacity, such as the formation of Cd-GSH complexes or inhibition of antioxidative enzymes (33). Despite extensive literature regarding Cd-induced ROS and mitochondrial dysfunction, the involvement of Cd-CL interactions has not been considered.

In this study, a novel mechanism for Cd-induced mitochondrial dysfunction is reported. Cd electrostatically releases proapoptotic cytochrome *c* from CL in parallel to IMM rigidification, loss of fully-assembled respiratory SCs, increased H_2O_2, and cytotoxicity that were reversed by the CL-binding drug MTP-131 / SS-31 / elamipretide or increased CL, revealing putative therapeutic strategy for chronic Cd intoxication, and potentially for other CL-interacting metals.

MATERIALS AND METHODS

Cell culture, transient transfection, and treatments

An immortalized cell line from the S1 segment of the human renal proximal tubule (HPCT-05-wt) was cultured as previously described (34). Myc-DDK-tagged *hCRLS1* plasmid (#RC213826, OriGene Technologies, Rockville, MD) or pCMV6-entry empty vector (EV) (#PS100001) were transiently transfected for 24 h using Lipofectamine 2000 (Invitrogen), according to manufacturer's instructions.

Metals ($CdCl_2$, $NiCl_2$, Sigma-Aldrich, Missouri, MO) were incubated in serum-free medium (SFM) to prevent binding to serum proteins. When used, MTP-131 (elamipretide, SS-31) (Cayman Chemical Company) was pretreated for 1 h in cells or for 15 min in isolated organelles. The antioxidants α-tocopherol (50 μM) and Tempol (1 mM) were preincubated for 1 h.

Isolation of organelles from HPCT cells

HPCT cells (4×10^6 in 8 T–175 flasks, 80%–90% confluency) were washed in ice-cold PBS, harvested using a rubber policeman, and pelleted at 600 *g* for 5 min at 4°C. Plasma membranes: After the removal of microsomes from cells ruptured by nitrogen decompression at 350 psi for 3 min in a cell disruption vessel (Parr Instruments), plasma membranes were collected by ultracentrifugation on a discontinuous sucrose gradient as described (35). Lysosomes: Cells were homogenized by Potter-Elvehjem and lysosomes were isolated using an OptiPrep gradient and ultracentrifugation (#89839, Pierce) (36). Mitochondria: A crude 9000 *g* mitochondrial fraction was isolated from cell lysates (#89874, Pierce).

Loading of membrane fluidity-reporting dyes

Unless otherwise specified, 6-dodecanoyl-N,N-dimethyl-2-naphthylamine (laurdan; #850582P, Avanti Polar Lipids), di-4-ANEPPDHQ (ANEPP; #50290, Potentiometric Probes) or diphenylhexatriene (DPH; #D208000, Sigma-Aldrich) linked to phosphatidylcholine (DPH-PC) (Rane Pharmaceuticals) were dissolved in DMSO and added after metal incubation. The volume of DMSO in the final solution did not exceed 1% of the total sample volume. For microscopy, laurdan (1 μM) and ANEPP (50 nM) were incubated for 15 min at 37°C and washed with PBS prior to imaging. For spectroscopy, laurdan (1:500 laurdan:lipid) or 16:0 DPH-PC (1:550 DPH-PC:lipid) was incubated at 37°C overnight or for 30 min, respectively.

Laurdan generalized polarization (GP)

Laurdan fluorescence (37) was measured as reported in (12) using either a Cary Eclipse spectrophotometer (Agilent Technologies) for nanoliposomes or a LS50B fluorescence spectrometer (PerkinElmer) for cellular membranes at λ_{ex} 340 nm and λ_{em} 440/490 nm (averaged of 3 technical replicates). Both excitation and emission bandwidth slits were set to 5 nm, and samples were loaded into small-volume quartz cuvettes (Starna Scientific, Ltd). Laurdan GP was calculated as described (12, 36).

DPH anisotropy

DPH is highly hydrophobic, adopts a flat, linear structure, and reports membrane fluidity based on the dynamics of the acyl chains in the hydrophobic core (38). Samples were illuminated with polarized light ($\lambda_{ex}/\lambda_{em}$ 360/430 nm) and DPH mobility changes were used to calculate steady-state fluorescence anisotropy (r). Higher r values indicate reduced DPH mobility compared to lower r values for the more fluid liquid-crystalline phase (39).

Multiphoton microscopy

Laurdan-stained HPCT cells were imaged using a Bergamo upright multiphoton microscope (Thorlabs) equipped with a fast-tuning Ti:Saph laser, high-sensitivity GaAsP detectors, and a 20x dipping objective lens and captured using a spectral filter (λ_{em} 420-730 nm). The resulting images were scaled and quantified using FIJI/ImageJ (40).

Laser scanning confocal microscopy

ANEPP-loaded HPCT cells in live-cell imaging chambers (ibidi GmbH) were spectral imaged (λ_{em} 490-750 nm) with

λ_{ex} 488 nm using a Nikon A1R+ inverted confocal microscope equipped with epi-fluorescence Ti2 illuminator, high-resolution Galvano scanner, CFI Plan Apochromat Lambda 60x oil objective, and collected using high sensitivity photomultiplier tube detectors. Slices corresponding to λ_{em} 570/620 nm were analyzed using FIJI/ImageJ.

Isolation of rat kidney cortex mitochondria and mitoplasts

All experiments were conducted following the EU Directive 2010/63/EU (internal reference 8775-2023-003). Male Sprague Dawley rats (250–300 g; Janvier Labs) were sacrificed by CO_2 inhalation and kidneys were excised into ice-cold MSH buffer (70 mM sucrose, 210 mM mannitol, 5 mM HEPES, pH 7.5) + 1 mM EDTA. The capsule was removed and the outer 2–3 mm cortex tissue was separated from the medulla. Crude rat kidney cortex mitochondria (rKC_{mito}) and mitoplasts, devoid of outer mitochondrial membrane (OMM), were isolated by motor-driven Potter-Elvehjem homogenization and differential centrifugation essentially as previously described (23, 25). Mitoplasts were prepared from mitochondria by digitonin permeabilization as described by Greenawalt (41) with slight modifications, as previously reported (23). Mitochondria and mitoplasts were used for experiments within 2 h post-isolation.

Solubilization of oxidative phosphorylation complexes and blue-native polyacrylamide gel electrophoresis (BN-PAGE)

PBS-washed cell pellets were processed according to (42). Briefly, plasma membranes were solubilized with 0.8 mg/ml high-purity digitonin (#300410 Merck) for 10 min on ice, stopped by dilution with PBS, and centrifuged at 20,000 *g* for 5 min at 4°C. Complexes in cell culture samples (125 µg) or rKC_{mito} (50 µg) were solubilized in 6 mg digitonin/mg protein from freshly prepared 20% high-purity digitonin (42, 43), incubated for 10 min on ice with inversion every minute, and centrifuged at 20,000 *g* for 30 min at 4°C. Solubilized proteins in the supernatant were mixed with 10X sample buffer, loaded onto precast 3%–12% NativePAGE Bis-Tris gels (Thermo Fisher Scientific), and electrophoresed at 4°C at 40 V for 1.5 h with 0.02% Coomassie blue G-250 cathode buffer (15 mM Bis-Tris, 50 mM tricine, 0.02% Coomassie blue G-250) followed by 30 V for 16 h in 0.002% Coomassie blue G-250 cathode buffer.

SDS-PAGE and immunoblotting

Samples were separated by SDS-PAGE under reducing and denaturing conditions, transferred onto PVDF membrane using Trans-Blot Turbo (Bio-Rad Laboratories), immunodetected as described (23) (supplemental Table S1), and visualized with chemiluminescence. Densitometric analysis was performed with Image Lab (v.6.1; Bio-Rad Laboratories) or FIJI/ImageJ.

Amplex UltraRed H_2O_2 assay

H_2O_2 was quantified utilizing 4 U/ml horseradish peroxidase (Sigma-Aldrich) and 10 µM Amplex UltraRed (Thermo Fisher Scientific) in an Infinite M Plex spectrofluorometer (Tecan Group) at $\lambda_{ex}/\lambda_{em}$ 545/590 nm. rKC_{mito} (0.03 mg) in MSH buffer + 1 mM EDTA (23, 25) were energized with 5 mM Na-succinate. Slopes were analyzed from normalized fluorescent intensities about 15 min after $CdCl_2$.

Dihydrorhodamine 123 assay

Dihydrorhodamine 123 (DHR123; Cayman Chemical Company) is oxidized to fluorescent rhodamine 123^+ ($Rh123^+$). The assay has been reported elsewhere (32).

Osmotic mitochondria swelling assay

Changes in volume of energized mitochondria due to colloid-osmotic effects of solute flux into the mitochondrial matrix following the addition of salts and modulators were monitored by the change in absorbance at λ_{540nm}. Kinetic measurements were carried out as previously reported (23, 25). Mitochondrial suspensions were separated by centrifugation at 10,000 *g* for 5 min at 4°C. Proteins in supernatants were precipitated with 20% trichloroacetic acid overnight at 4°C, centrifuged at 10,000*g* for 5 min at 4°C and neutralized with 8 M urea, 2% SDS, 10 mM DTT, 65 mM Tris, pH 9.5. Samples were sonicated and analyzed by immunoblotting.

ATP assay

ATP was determined using ATPlite 1step (PerkinElmer), according to the manufacturer's instructions. ATP concentration in unknown samples was determined using linear regression of known standards and corrected for protein.

MTT cell viability assay

MTT assay was performed as previously described (23), according to the optimized method by Denizot and Lang (44).

Nanoliposome preparation

Lipid films for pure tetramyristoyl-CL (TMCL; T_m 28–40°C) or IMM biomimetic (45) nanoliposomes (palmitoyl-oleoyl-phosphatidylcholine (POPC, 40 mol %), dioleoylphosphatidylethanolamine (DOPE, 35 mol %), tetraoleoyl-CL (TOCL, 20 mol %), and stearoyl-arachidonoyl-phosphatidylinositol (SAPI, 5 mol %)) (Avanti Polar Lipids) were prepared, rehydrated and used to form nanoliposomes by extrusion, essentially as described by Kerek *et al.* (12). Films were rehydrated using 1 ml HEPES buffer (20 mM HEPES, 100 mM NaCl, pH 7.4). Multi-lamellar vesicles (MLVs), formed by rigorous sonication and 5 cycles of freeze-thawing, were passed through a Nucleopore polycarbonate filter with 100 nm pore diameter using a mini-extruder at 45°C (Avanti Polar Lipids) to form large unilamellar vesicles (LUVs). Lipid concentration following extrusion was determined using a phosphate assay (46). Nanoliposomes (0.1 mM) were incubated for 5 min with $CdCl_2$ and/or 0.1 mM MTP-131.

Dynamic light scattering and zeta potential

Liposome size and size distribution were assessed at 37°C as reported previously (10, 12, 28). Zeta potential provides a means of determining liposome stability (±30 mV). Charged liposomes will attract layers of opposite charge around their surface, separating them from the bulk solvent. Zeta potential measures the electrical potential difference between the bulk and the slipping plane, which denotes the location at which the attracted ions of opposite charge can no longer be differentiated from the bulk solvent (47).

Quantitative analysis of nanoliposome fusion size change criteria

Based on lipid molecular area and approximate lipid number in the outer membrane leaflet (OML) of spherical vesicles with 100 nm diameter, an estimated 51.5% of total lipid molecules reside in the OML (48). Using average molecular areas and lipid composition for IMM biomimetics, the weighted average molecular area was 77.135 $Å^2$ with a diameter of 113 nm (1,130 Å). The total area can be calculated by:

$$A = 4\pi r^2 \quad (1)$$

where A = area, r = radius. A divided by average lipid molecular area estimates 52,006 OML lipids. Complete fusion of two liposomes would result in 104,111 OML lipids with predicted diameter of 159.8 nm, therefore a size increase of >46.8 nm is required (49).

Lipid extraction

Lipid extraction was performed from 50-100 μg HPCT homogenates using a modified Folch method (50) and included the addition of 1.9 nM TMCL (Avanti Polar Lipids) as an internal standard. After phase separation and centrifugation, the organic phase was dried under nitrogen gas.

Cardiolipin analysis by LC-MS/MS

Stock solutions (1 mg/ml in chloroform) of bovine heart CL (90% tetralinoleoyl-CL [TLCL], 18:2-CL) and TMCL (Avanti Polar Lipids), used for the standard curve and as internal standard, respectively, were diluted with 0.1% NH_4OH in methanol:water (90:10, v/v) (51). Unknown cell samples were injected and separated on an Xtimate C4 column (3 μm, 2.1 × 150 mm; Welch Materials) with an Xtimate C4 precolumn (3 μm, 2.1 × 10 mm; Welch Materials) at a flow rate of 0.5 ml/min using a solvent gradient program for elution (supplemental Table S2). The column oven was 45°C and samples were cooled to 4°C in the autosampler. An LC-MS/MS system consisting of a Nexera LC-40 UHPLC (Shimadzu) coupled with a 6,500+ triple quadrupole mass spectrometer (SCIEX) was run in ESI negative mode. The source parameters were as follows: ion source gas 1 50 psi, ion source gas 2 70 psi., curtain gas 25 psi, CAD gas 7 source temperature 500°C, spray voltage 4,500 V.

Quantification was performed in the multiple reaction monitoring (MRM) mode, which was optimized by infusing standard solutions at 1 ng/ml (supplemental Table S3). Data processing and quantitation were performed by SCIEX OS v.3.1.0.16485. Linear regression was used for calibration, wherein the ratio of the peak areas of TLCL:TMCL was plotted against TLCL concentration.

Statistical analyses

Unless specified otherwise, all experiments were biologically replicated at least three times and presented as representative data or means ± SD. Unpaired two-tailed Student's t test was used for pairwise comparisons. For comparisons involving more than two groups, statistical distinctions were assessed using one-way ANOVA, assuming equality of variance, followed by Tukey or Dunnett post-hoc test using GraphPrism (v.9.1.1) or SigmaPlot 14.0. Results with $P \leq 0.05$ were considered statistically significant where $^*P < 0.05$, $^{**}P < 0.01$, $^{***}P < 0.001$, $^{****}P < 0.0001$.

RESULTS

Defining and measuring membrane fluidity

The term membrane fluidity is very broad and not well defined for a complex biological membrane. In the context of this study, fluidity is understood as a change in lipid packing with more or less ordering (fluid or rigid). Less packing and reduced order of the chains allow more water penetration and the solvent-sensitive dye laurdan is well-suited to measure these changes as a reflection of membrane fluidity.

Due to its naphthalene moiety and long non-polar 12-carbon lauryl tail, the amphiphilic nature of laurdan tethers it at the interface between phospholipid head groups and initial C atoms of fatty acid tails (**Fig. 1**A), probably flipping between the two membrane leaflets. In addition, we use the hydrophobic dye DPH to measure fluorescence anisotropy in the membrane core, which directly reflects the mobility of the dye as a function of more or less order in the acyl chains (Fig. 1A).

Di-4-ANEPPDHQ (ANEPP) is better retained in the OML (Fig. 1A) and distributes to liquid-ordered/rigid or liquid-disordered/fluid lipid domains, which are discerned by different emission spectra. Finally, NR12S, a lipid environment-sensitive Nile Red-derived probe that accumulates in cholesterol-rich membrane domains and exhibits little flip-flop between membrane leaflets (52), was employed in supplemental Fig. S1. Emission wavelengths <585 nm (blue range) are indicative of liquid-ordering whereas >585 nm (red range) depict liquid-disordering and the blue/red ratio increases with increasing membrane stiffening.

Membrane rigidification by Cd in isolated organelles

Cd interactions with membranes can affect their fluidity with consequences on membrane protein function and downstream signaling pathways. Using Cd-exposed HPCTs to model Cd nephrotoxicity, membrane fluidity reported by laurdan was measured in isolated membranes. To determine whether changes in membrane fluidity are Cd-specific, a further divalent cationic toxic metal Ni (0.1 mM) was used for comparison. As previously reported (10, 36), both Cd and Ni caused rigidification of plasma membranes (Fig. 1B) and fluidization of lysosomal membranes (Fig. 1C). Despite Ni^{2+}'s smaller size and higher electronegativity than that of Cd^{2+} (1.91 for Ni^{2+} vs. 1.69 for Cd^{2+}, Pauling scale), whole mitochondria exhibited fluidization by Cd but not by Ni (Fig. 1D), implying membrane composition is critical for toxic metal-lipid interactions.

Laurdan may not detect all fluidity changes in the convoluted IMM. Thus DPH, which inserts into the highly-disordered hydrophobic core (Fig. 1A), was also used in mitoplasts, verified by reduction of OMM voltage-dependent anion channel (VDAC) and

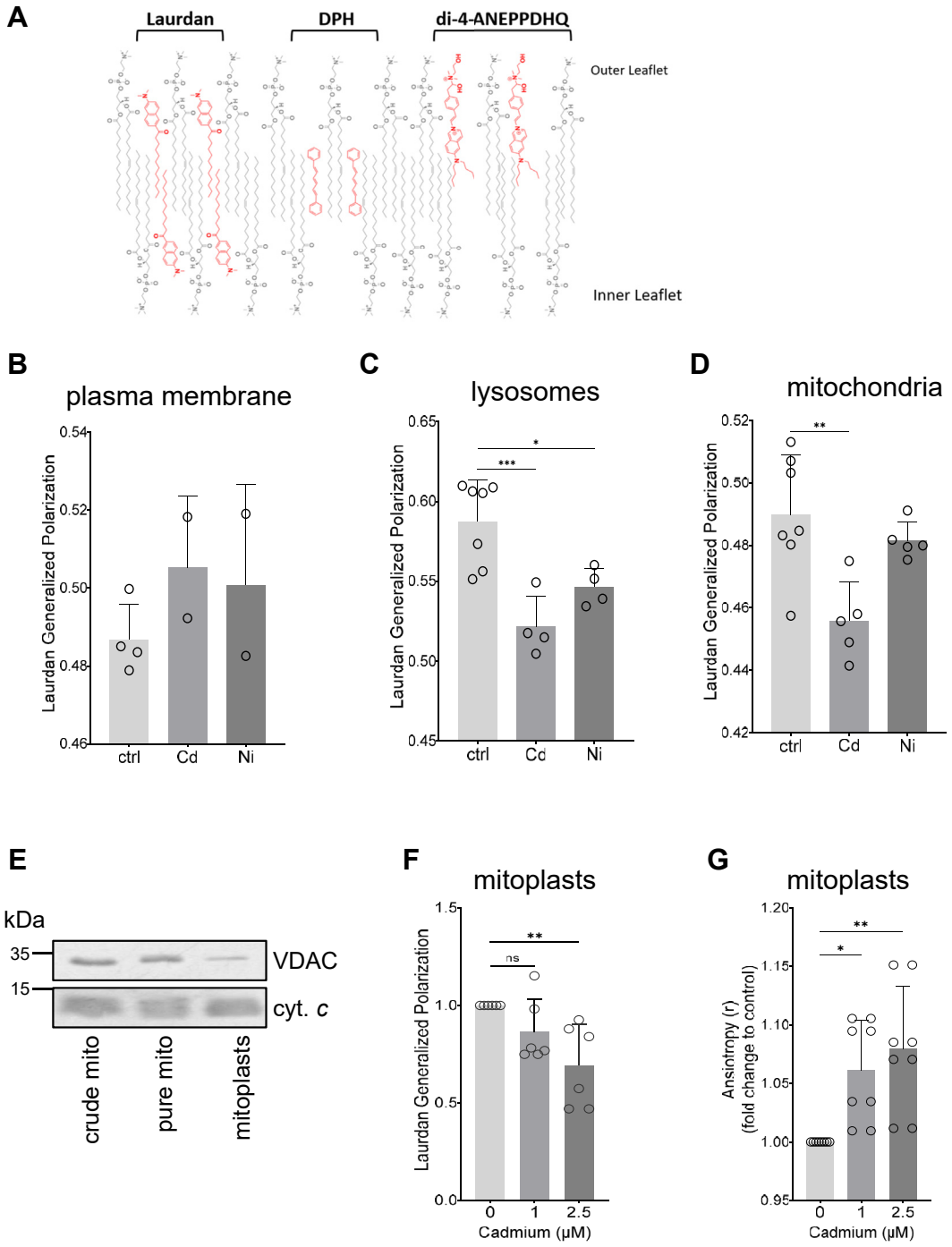

Fig. 1. Alterations in fluidity of isolated cellular membranes by cadmium. A: Depiction of membrane fluidity-reporting fluorophores (laurdan, diphenylhexatriene [DPH], di-4-ANEPPDHQ) interaction with a model membrane (not to scale). Human proximal tubule (HPCT) cells were exposed to 2.5 μM $CdCl_2$ (Cd) or 0.1 mM $NiCl_2$ (Ni) for 6 h in serum free medium (SFM). Plasma membranes (B), lysosomes (C), and mitochondria (D) were isolated as described in Materials and Methods, loaded with 1:550 laurdan:lipid, incubated overnight at 37°C and measured at $\lambda_{ex}/\lambda_{em}$ 340/440 nm and 340/490 nm. Laurdan generalized polarization (GP) was determined, where increased GP indicates liquid-ordered membranes and decreased GP indicates membrane fluidization. Data were measured in technical triplicate from at least two independent isolations. E: Quality control of mitoplast preparations from rat kidney cortex mitochondria (rKC_{mito}) as depicted by loss of outer mitochondrial membrane protein (OMM) VDAC and retention of inner mitochondrial membrane (IMM) cytochrome c (cyt. *c*). Immunoblot is representative of 4 independent experiments. Mitoplasts were exposed to Cd for 1 h and loaded with laurdan (F) or DPH (G). Increased DPH anisotropy indicates membrane rigidification. Data were generated in technical triplicate from 6 to 8 independent mitoplast preparations.

retention of IMM cytochrome *c* (Fig. 1E). Membrane fluidity reported by laurdan GP was increased in mitoplasts by Cd (Fig. 1F), supporting observations in mitochondria (Fig. 1D), whereas DPH anisotropy was augmented, indicating rigidification of the IMM hydrophobic core (Fig. 1G). Similarly, the NR12S membrane fluidity-reporting probe was used in rKC_{mito} and mitoplasts (supplemental Fig. S1). As a positive control, mitochondria were treated with digitonin to disrupt cholesterol-rich domains (53), resulting in an expectant decrease in the blue/red ratio interpreted as increased membrane fluidity (supplemental Fig. S1A). While intact Cd-exposed mitochondria exhibited slight increase in the blue/red ratio, and thus in liquid-ordering and membrane rigidification, this was even more apparent in Cd-treated mitoplasts (supplemental Fig. S1B–D), which is in line with the DPH observations in Fig. 1G. Thus, these data imply Cd increases fluidity at the polar surface of membranes whereas the hydrophobic core becomes more rigid.

HPCT intracellular membrane fluidity is decreased by Cd

Multiphoton live-cell imaging of 1 h Cd-treated and laurdan-loaded HPCT cells evidenced increased signals at 440 nm and concomitant decrease at 490 nm (**Fig. 2**A). Increases in blue fluorescence (i.e. rigidity) were observed in well-defined vesicles (Fig. 2A, arrows) in the perinuclear region, cell periphery, and blebbing membranes (Fig. 2A, arrowheads). Single-cell quantification evidenced elevated laurdan GP, and thus membrane rigidity evoked by 1 μM Cd (Fig. 2B).

ANEPP distributes to liquid-ordered/rigid (λ_{em} 570 nm) or liquid-disordered/fluid (λ_{em} 620 nm) lipid domains. In control cells, λ_{em} 620 nm ANEPP signals were strongly localized in rod-like structures, indicative of mitochondria (Fig. 2C, left, arrowheads), and in cell membranes (Fig. 2C, left, arrows) whereas λ_{em} 570 nm signals were found in smaller vesicular structures (Fig. 2C). In Cd-treated HPCT, both fluorescence intensities were reduced by ∼50% (Fig. 2D, E) and increased ratio of 570/620 nm in Cd-treated HPCTs over controls indicated loss of λ_{em} 620 nm was greater (Fig. 2F), particularly in mitochondria (Fig. 2G), suggesting reduced liquid-disordered domains (Fig. 2F), and supporting the data from mitoplasts (Fig. 1G, supplemental Fig. S1D).

CL nanoliposomes are rigidified by Cd

As one of the most abundant lipids in the IMM, we drew our attention to CL. With two negative charges at physiological pH, we hypothesized Cd interacts directly with CL (12), potentially altering CL structure through an increase in hydrophobic tail volume and decreasing the distance between the phosphoglycerol head groups generating an exaggerated conical form (Fig. 2H, right), in a similar fashion to Ca^{2+} (54). In a reductionistic approach devoid of interfering phospholipids and membrane curvature, Cd right-shifted the phase transition temperature (T_m) of laurdan-preloaded pure 14:0 CL (TMCL) nanoliposomes by ∼1°C (Fig. 2I), thus translating to significant decrease in membrane fluidity (Fig. 2J).

Disruption of mitochondrial SC assembly and ROS by Cd is reversed by the CL aggregator, MTP-131

Since ROS generation and oxidative stress are integral components of Cd effects, we hypothesized Cd-CL causes SC disruption and generation of detrimental ROS levels through membrane rigidification. SC $I+III_2+IV_n$ (predicted size 1.2 MDa) assembly was prevented by ∼30% after Cd exposure in CI, CIII, and CIV immunoblots (**Fig. 3**A, B), with unaltered total complex expression (supplemental Fig. S2A). Similar observations were made in rKC_{mito} (Fig. 3C). In mitoplasts, III_2+IV_2 and III_2+IV_1 SCs were diminished by Cd (supplemental Fig. S3), reiterating Cd's negative effect on SCs. Potentially, lipid peroxidation by Cd-induced ROS, rather than a direct association of Cd with lipids, could underpin SC disruption. The superoxide dismutase mimetic Tempol (supplemental Fig. S4) and the fat-soluble antioxidant α-tocopherol (vitamin E) (Fig. 3D, E) were ineffective in reversing SC disruption by Cd, further strengthening the hypothesis of direct Cd-CL interaction, rather than lipid peroxidation, as the underlying mechanism.

To better understand Cd-CL and IMM fluidity, IMM biomimetic nanoliposomes (45), which were preincubated with Cd prior to laurdan, resulted in increased membrane rigidity across the entire temperature range as depicted by a right-shift (Fig. 3F) and higher laurdan GP at physiological temperature of 37°C (Fig. 3G), which is in line with previous observations in anionic membranes (phosphatidic acids and phosphatidylserines) (55), and is predominately attributed to electrostatic interactions. Although zwitterionic lipids comprise 75% of the lipids in this IMM biomimetic model, binding of Cd is still observed due to CL, which remains the bulk of the anionic portion, because it carries two phosphate moieties that are readily accessible to Cd. Despite seemingly contradictory to membrane fluidization by Cd in laurdan-loaded mitoplasts (Fig. 1F), IMM biomimetics are devoid of proteins, which also influence membrane biophysics (56).

Elamipretide / MTP-131 / SS-31 is a small mitochondrially-targeted CL-binding tetrapeptide (57, 58) that hinders membrane surface electrostatic interactions (59). We reasoned MTP-131 should prevent Cd-induced disruption of SC assembly, possibly by competing with Cd for CL interaction. Nanomolar MTP-131 abolished Cd-perturbed SCs (Fig. 3H, I), without altering total complex abundance (supplemental Fig. S2B). Cellular ATP was diminished with 5 μM Cd after 24 h (Fig. 3J), yet no difference in Cd-treated cells occurred with MTP-131 (Fig. 3K), thus ATP generation is not detrimentally affected as well as

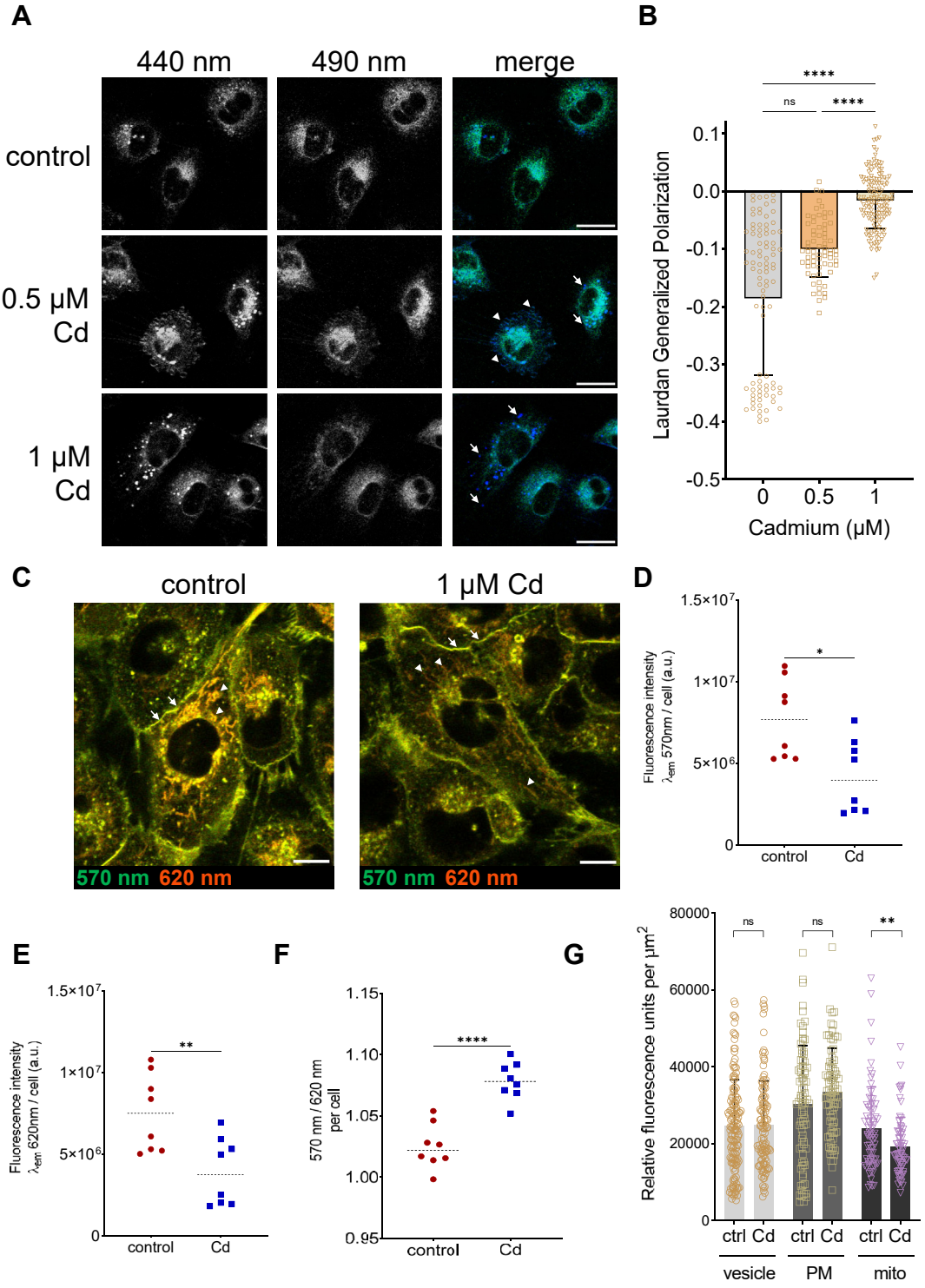

Fig. 2. Cadmium augments mitochondrial membrane rigidity in HPCT cells and CL nanoliposomes. After exposure to $CdCl_2$ for 1 h, HPCT cells were loaded for 15 min at 37°C with 1 µM laurdan (A) or 50 nM di-4-ANEPPDHQ (C) and imaged after washing. A: Laurdan-loaded cells were imaged at $\lambda_{ex}/\lambda_{em}$ 340/440 nm and 340/490 nm using a multiphoton microscope. Elevated membrane rigidity is indicated by increased λ_{em} 440 nm and decreased λ_{em} 490 nm that was observed in intracellular vesicles (arrows) and in circular membrane structures (arrowheads). Scale bar = 20 µm. B: Quantification of single-cell laurdan GP from 90 (control), 68 (0.5 µM Cd), and 139 (1 µM Cd) cells from three independent experiments. C: Cells loaded with di-4-ANEPPDHQ were spectral imaged on a laser-scanning confocal microscope with a 488 nm excitation laser. A spectral shift occurs when di-4-ANEPPDHQ distributes to liquid-ordered (λ_{em} 570 nm) or to liquid-disordered (λ_{em} 620 nm) lipid domains. Plasma membrane (arrows) and mitochondria (arrowheads) are indicated in representative images. Scale bar = 20 µm. D and E: Fluorescent intensities from eight images per condition containing 339 (control) and 417 (Cd) cells were analyzed from two independent experiments and divided by cell number. F: Ratios of 570–/620 nm using the values obtained in (D and E) are plotted (n = 8 images). G: Fluorescence signals at λ_{em} 620 nm were quantified in vesicular structures, plasma membrane (PM) and mitochondria of control and Cd-treated HPCT cells. At least 70

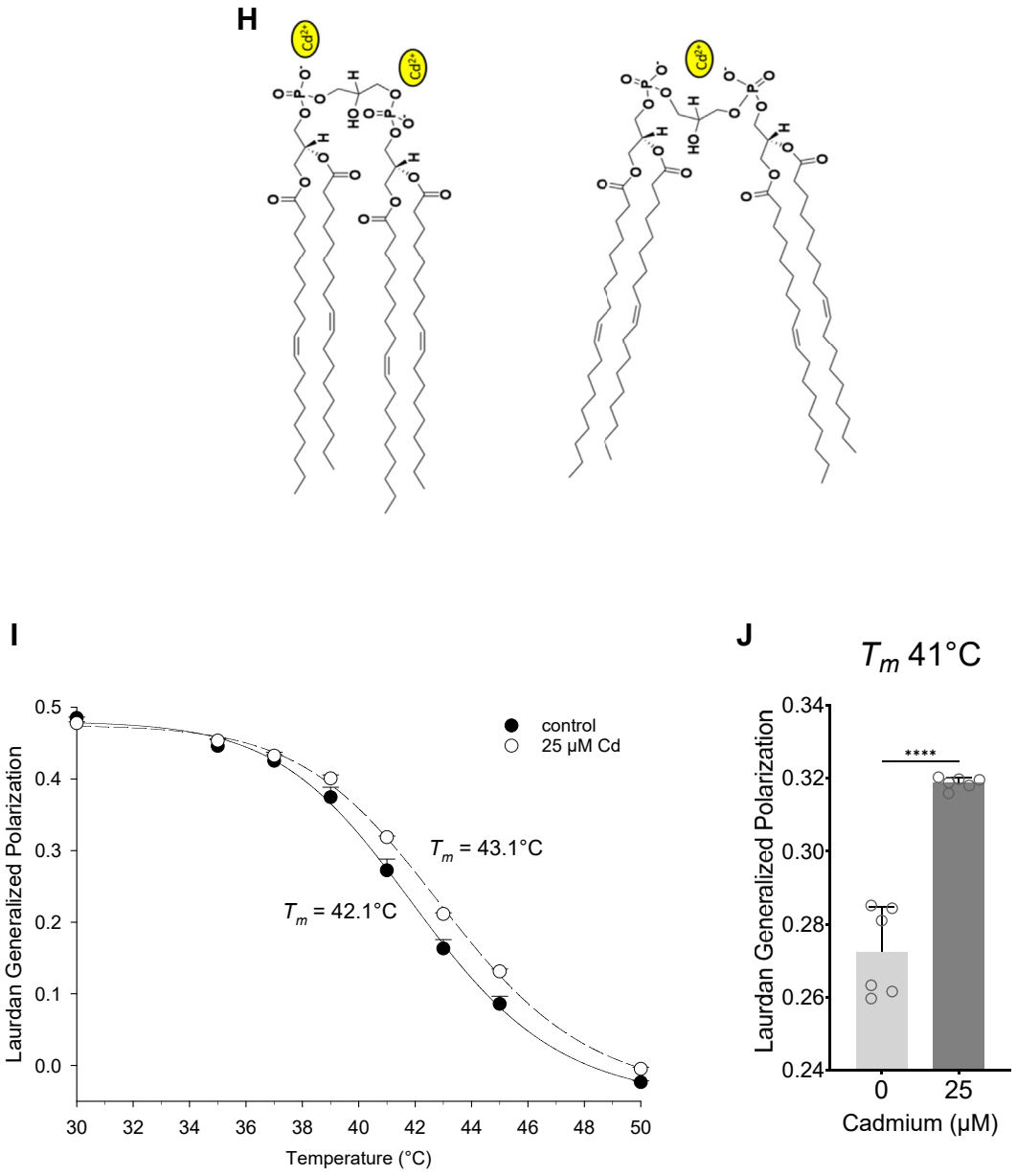

Fig. 2. Continued.

indicating additional Cd targets in mitochondria, such as the Q_o site of CIII (27) or aquaporin-8 (23).

When CI is free and not incorporated in a respiratory SC, H_2O_2 generation is elevated (17). Energized rKC_{mito} increased H_2O_2 after Cd addition (**Fig. 4**A) that was ablated by pretreatment with MTP-131 (Fig. 4B, C), and was also reproduced in HPCT cells by DHR123 oxidation (Fig. 4D). Slope analysis of the Amplex UltraRed curves evidenced significant MTP-131 attenuation of H_2O_2 increase by 2.5 μM and 5 μM Cd (Fig. 4C).

Cd-induced mitochondrial swelling is not affected by MTP-131

Mitochondrial swelling by Cd (23, 26) was recapitulated in this study using $CaCl_2$ + KH_2PO_4 as a positive control (**Fig. 5**A, B). Higher Cd (5 μM) evokes less

regions per condition in 40–60 cells from 4 independent images were used. H: Structures of tetraoleoyl-cardiolipin (TOCL) were drawn using ChemDraw. (left) Cadmium (Cd^{2+}) electrostatic interaction with each phosphate headgroup (monodentate binding) neutralizes negative charges dissipating charge repulsion. (right) Putative bidentate binding of Cd^{2+} with both phosphate headgroups. Drawings are not to scale. I: Phase transition of pure TMCL nanoliposomes with laurdan. Nanoliposomes preloaded with laurdan were measured before and 5 min after Cd addition. J: Comparison of laurdan GP at CL phase transition temperature before and after Cd addition. Measurements were performed in triplicate from two independent nanoliposome preparations.

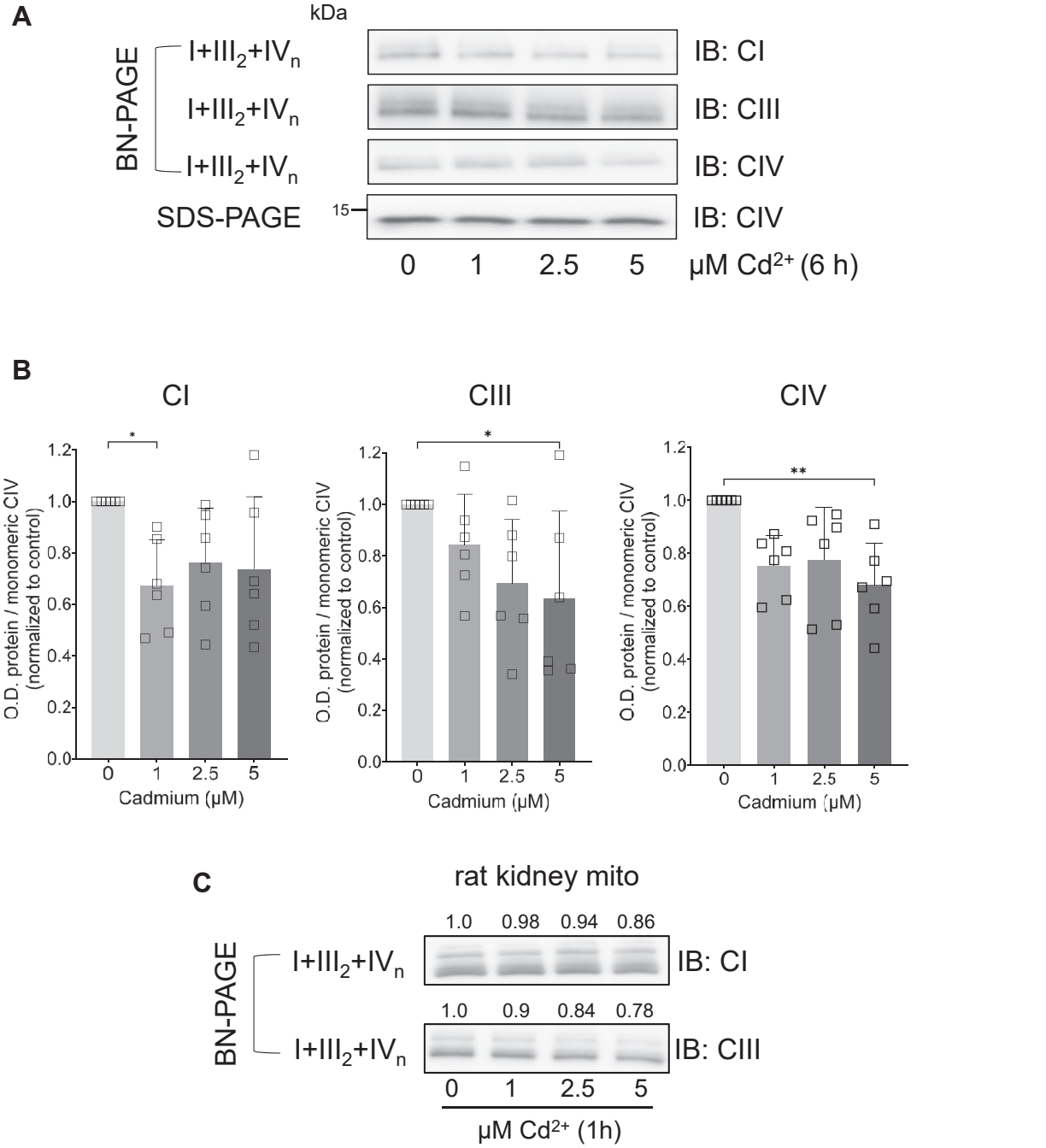

Fig. 3. Ablation of cadmium-perturbed mitochondrial respiratory supercomplexes assembly by MTP-131, Human proximal tubule (HPCT) cells (A, B) or isolated crude rat kidney mitochondria (rKC_{mito}) (C) were exposed to 1, 2.5 and 5 µM $CdCl_2$ (Cd) for 6 h in SFM or for 1 h in MSH buffer, respectively. Cell pellets and isolated organelles were processed as described in Materials and Methods and separated by BN-PAGE using total monomeric complex IV to control for loading. Immunoblotting (IB) was used to visualize the mitochondrial supercomplexes (SCs). Representative immunoblots from n = 6 in (A) are shown. B: Densitometry analysis of complex I (CI), complex III (CIII) and complex IV (CIV) signals corrected for loading and normalized to control show a significant reduction of fully assembled SCs (n = 6). C: Representative BN-PAGE followed by IB from n = 3 of isolated rKC_{mito}. Relative optical densities normalized to control show a reduction of fully assembled SCs following Cd exposure. D: The antioxidant α-tocopherol (α-toco; 50 µM) was preincubated for 1 h prior to 6 h Cd treatment. SC formation was assessed by BN-PAGE and IB. Representative immunoblots from n = 4 are shown. E: Densitometry analysis of IBs in (D) show no significant impact of α-tocopherol on SC loss by Cd. F: Laurdan GP in nanoliposomes (100 nm diameter) comprised of 40 mol % POPC, 35 mol % DOPE, 20 mol % TOCL and 5 mol % SAPI to mimic the IMM lipid composition. Laurdan was added after Cd addition. Means ± SD from replicate measurements from two independent nanoliposomes preparations are shown. G: At physiological 37°C, laurdan GP and membrane rigidification is increased by Cd (n = 6–9). H: HPCT cells were pretreated with 0.1 µM MTP-131 for 1 h and exposed to 5 µM Cd for 6 h. Cell pellets were subjected to BN-PAGE followed by IB to visualize the SCs. A representative experiment from n = 4–5 is shown. I: Quantitative analysis of band optical density normalized to control shows protection by MTP-131 pretreatment (n = 4–5). J: Cd exposure of HPCT cells significantly reduces the ATP concentration only at 5 µM after 24 h (n = 4). K: Pretreatment with 0.1 µM MTP-131 has no effect on ATP concentrations by 24 h Cd (n = 6).

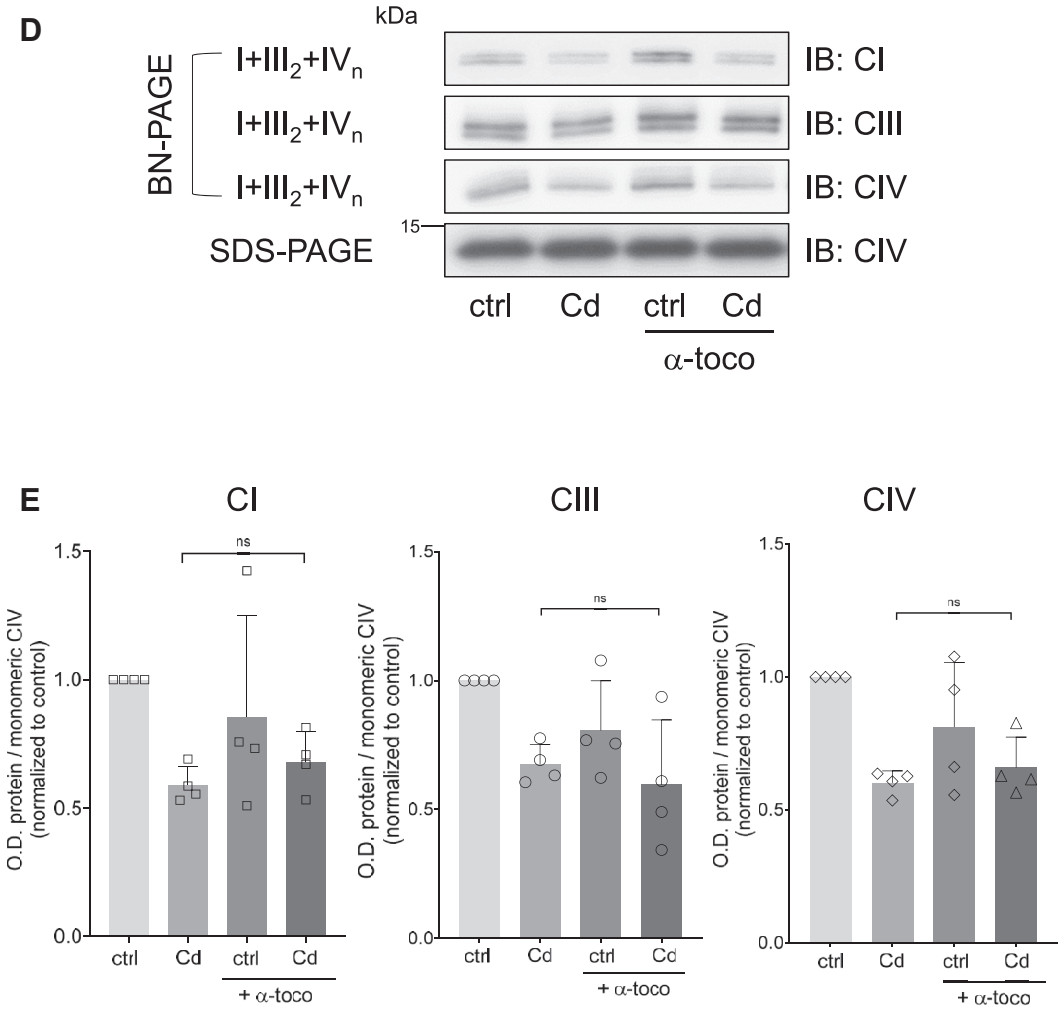

Fig. 3. Continued.

swelling, possibly due to activation of contraction dynamics driven by K^+/H^+ exchange (25). Intriguingly, MTP-131 was ineffective on osmotic swelling (Fig. 5A, B), but dampened Cd-induced cytochrome *c* release from the mitochondrial pellet (Fig. 5C, D) (23), implying swelling is a CL-independent process whereas Cd-CL most likely disrupts cytochrome *c*-CL complexes (60), liberating it from mitochondria.

IMM nanoliposomes exhibit a rigid membrane state and increased size with Cd

Cd-lipid binding or shielding of CL charges by MTP-131 binding can be readily assessed by zeta potential (see Materials and Methods, **Fig. 6**A). Stable IMM nanoliposomes displayed a zeta potential of −28.5 mV indicating their stability (47) that was substantially reduced to −21.5 mV (Fig. 6B) after association with MTP-131, confirming drug binding and presumably saturating all CL binding sites to restrict lipid movement, as indicated by increased laurdan GP (Fig. 6C, D) and lack of nanoliposome size increase (Fig. 6E). Occlusion of CL interaction sites for Cd by MTP-131 prevents changes in zeta potential (Fig. 6B) and laurdan GP (Fig. 6C, D) by Cd.

Cd binding to key anionic lipids results in liposome size increase and aggregation (12), which could foster liposome fusion. Based on the molecular area of the lipids and the approximate number of outer leaflet lipids in the IMM mimic vesicles (see Materials and Methods), the fusion of two IMM nanoliposomes would result in a theoretical diameter increase of at least ∼46 nm. Cd-induced diameter increase of ∼40 nm (Fig. 6E) in IMM nanoliposomes is insufficient to predict liposome fusion (see Materials and Methods). Rather, the larger IMM biomimetic diameter with Cd (Fig. 6E) could result from bidentate binding of Cd with CL's two phosphate headgroups (Fig. 2H), triggering a conformational change that alters lipid packing, and potentially culminating in hexagonal phase transition (54). Restriction of lipid movement or inhibition of Cd binding by MTP-131 could explain the lack of IMM nanoliposome size increase in its presence (Fig. 6E), consistent with the observations of differential rigidification seen in Fig. 6C.

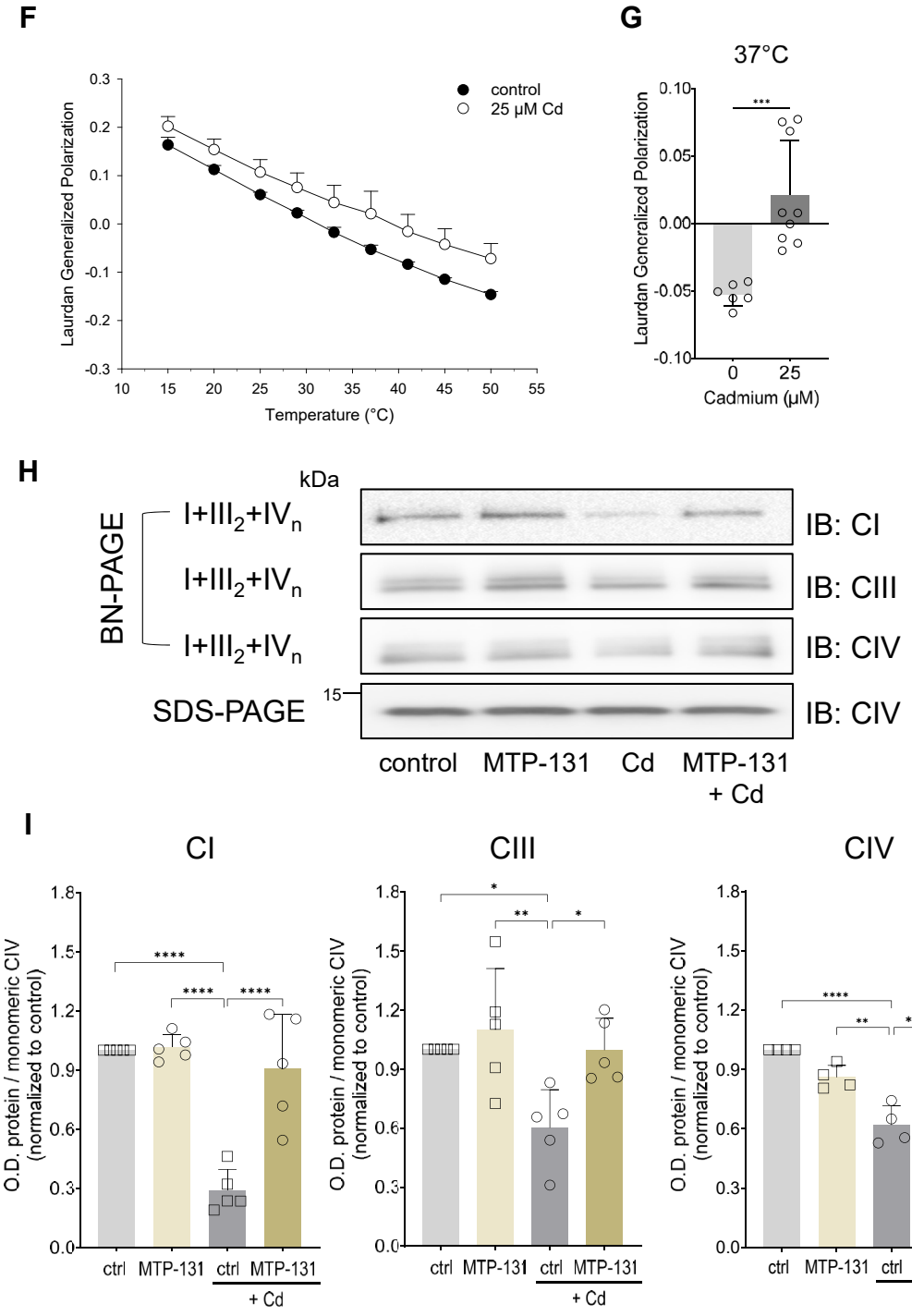

Fig. 3. Continued.

Increased CL-Cd ratio diminishes Cd-induced mitochondrial dysfunction and toxicity

Based on the inference that Cd-CL interactions disrupt membrane biophysics and prevent SC assembly, CL synthase 1 (gene *CRLS1*), which converts phosphatidylglycerol (PG) into CL, was overexpressed to increase the ratio of CL:Cd and thereby potentially prevents Cd effects by either directly buffering Cd ions or by increasing available CL for SC formation. Transfection efficiency in HPCT cells was validated by qPCR (**Fig. 7**A), where *CRLS1* mRNA was elevated by > 700-fold, and immunoblotting (Fig. 7B). Myc-DDK-tagged CRLS1 was observed at the expected molecular weights of ~35 kDa for transcript variant 1 (Fig. 7B, arrow) and ~22 kDa for transcript variant 2 (Fig. 7B, arrowhead). CRLS1-HPCT cells accrued ~50% more CL over empty vector (EV) controls (Fig. 7C) without noticeable cytotoxicity (data not shown). Cd toxicity

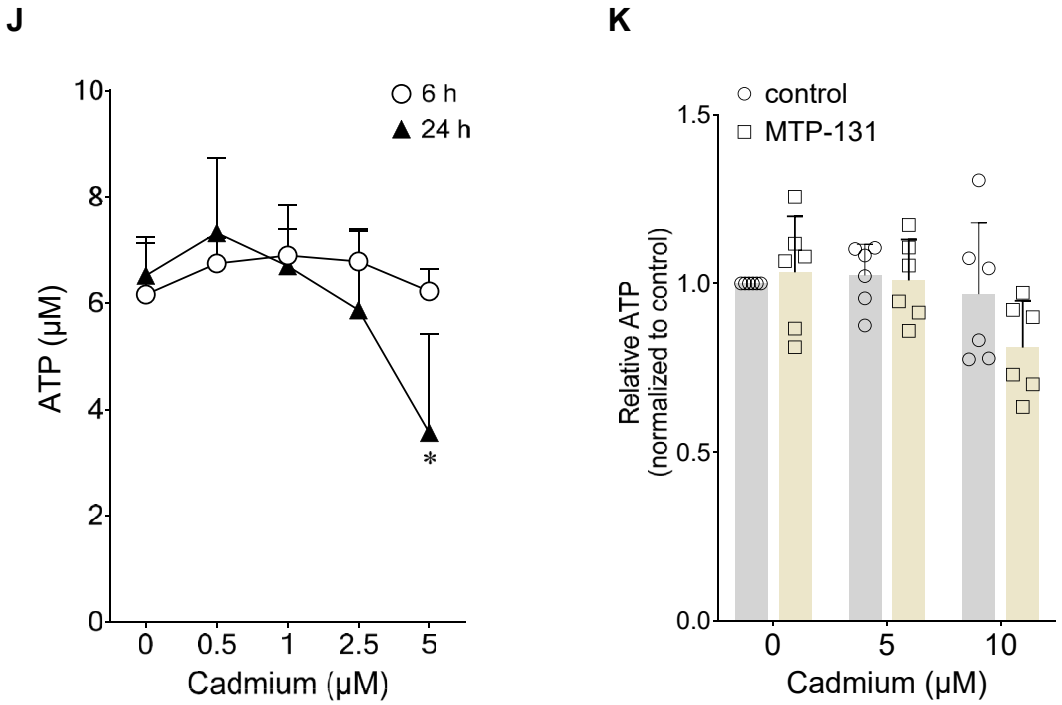

Fig. 3. Continued.

(Fig. 7D) and Cd-induced ROS generation (Fig. 7E) were abolished in CRLS1-HPCT. Intriguingly, Cd reduced ROS formation below that of control levels in CRLS1-overexpressing cells. The increased number of CL molecules will not only sequester Cd ions and scavenge ROS (becoming oxidized in the process), but CL may also alter the SC response to Cd-CL interaction, such as preventing ROS formation or activating an antioxidant response so that a decrease in ROS is observed.

Finally, in ANEPP-loaded HPCT cells expressing a 10-fold difference in *CRLS1* mRNA (supplemental Fig. S5), mitochondrial membrane rigidification by Cd was still evidenced at slightly increased CRLS1/CL levels but was abolished when CRLS1/CL exceeded a certain threshold (Fig. 7F), further evidencing the pivotal role of Cd-CL-ratio in Cd-induced mitochondrial dysfunction.

DISCUSSION

Metal pollution is an increasing global threat to human and environmental health, complicated by unpredictable weather patterns (61). Through consumption of contaminated food and water, humans accumulate Cd in the kidney over decades (7, 62). At the cellular level, toxic metals, such as Cd, elicit oxidative stress and potential cell death and/or transformation pertinent to mitochondrial dysfunction (63). Physiological and non-physiological cations electrostatically interact with negative charges on phosphate headgroups of phospholipids causing conformational change of targeted lipids and alterations in membrane architecture and fluidity, usually rigidification (64, 65). Here, we report a novel toxicological mechanism for Cd launched by direct interference with mitochondrial phospholipid CL.

ETC complexes and ATP-synthase dimers are found almost exclusively in infoldings of the IMM, the cristae (66). There, the protonmotive force and hence ATP are generated locally within the crista lumen. Both proteins, e.g. mitochondrial contact site and cristae organizing system (MICOS) (67), and lipids, such as CL (68), are crucial membrane-shaping factors and react to changing metabolic demands. Contrary to key cylindrical membrane bilayer-building blocks like PC, CL has a conical structure (**Fig. 2**H), accumulating at curved crista ridges, mostly in the OML, with its headgroups facing the crista lumen, forcing negative curvature of the IMM through mechanical buckling (31, 68) and membrane polymorphisms (69) (**Fig. 8**A). CL also prevents IMM curvature loss and accommodates the insertion of mitochondrial membrane proteins (70). The ability of CL to form hexagonal (HII) phases also depends on the nature of divalent ions, whereby Ca and Mg have stronger effects compared to Sr or Ba (71, 72). Based on the similarities outlined below, Cd is acting more like Ca.

Cd crosses the OMM through the divalent metal transporter 1 (DMT1) (73) or abundant VDAC followed by IMM permeation through the MCU (23) into the matrix and permitting Cd-CL interaction from both the intermembrane space and matrix/cristae lumen. Spatial CL disorganization by direct Cd-CL interaction could modify IMM/cristae organization and lipid

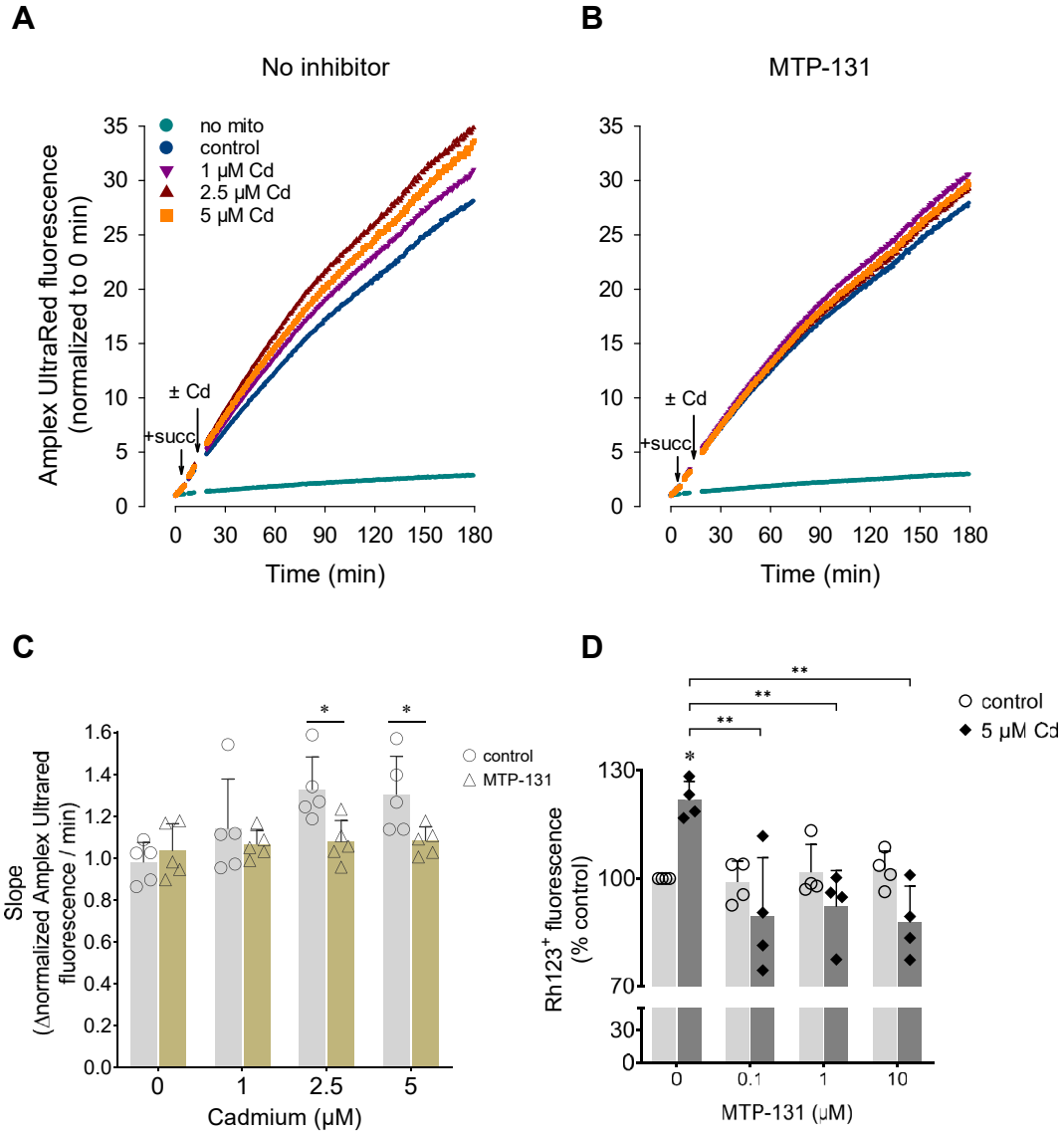

Fig. 4. MTP-131 abolishes elevated mitochondrial H_2O_2 by cadmium, Amplex UltraRed fluorescence of succinate-energized crude rKC_{mito} suspended in iso-osmotic MSH buffer was monitored at $\lambda_{ex}/\lambda_{em}$ 545/590 nm. A: Cd (1, 2.5, or 5 µM) was added 5 min after mitochondria were energized by 5 mM Na-succinate (succ). B: MTP-131 (0.1 µM) was preincubated for 15 min at RT. Representative experiments from n = 5 are shown in (*A*) and (*B*). C: Pretreatment with MTP-131 significantly reduced the rates of H_2O_2 release, determined by the slope of normalized fluorescence intensities during the first 15 min after Cd addition (n = 5). D: HPCT cells exposed to 5 µM Cd for 3 h in SFM show a significant reduction of ROS formation measured by fluorescence intensities of oxidized rhodamine 123^+ ($Rh123^+$) at $\lambda_{ex}/\lambda_{em}$ 485/535 nm (n = 4).

packing (74), and limit molecular proximity of ETC complexes for the formation of respiratory SCs (75), and exacerbate ROS formation, as clearly demonstrated in this study (Figs. 3, 4, and 8B). Hence, Cd appears to counteract CL membrane alterations, in particular reversing fluidity (Figs. 1 and 2), which is exemplified in ultrastructural studies of renal, hepatic and muscle mitochondria from Cd-exposed rats wherein cristae were regressed (76).

SCs exist in various states and combinations (77, 78), such as I_1+III_2+IV or III_2+IV_2, at any one time point, reflecting their high dynamic nature and biological plasticity to accommodate continuously changing metabolic demands during cellular processes as well as mediating and co-ordinating defense or adaptive stress responses. In contrast to the proposed "fluid-state" and "solid-state" models, the "plasticity" model includes the co-existence of ETC complexes as both single entities or part of respirasomes. Substantial evidence for SC formation and their central role in advantageous mitochondrial energetics, prevention of excessive ROS generation due to electron leakage from CI, and maintenance of proteins in the IMM (66) ascertain the physiological advantage of SCs.

The organization and assembly of ETC complexes into large respiratory SCs are dependent on

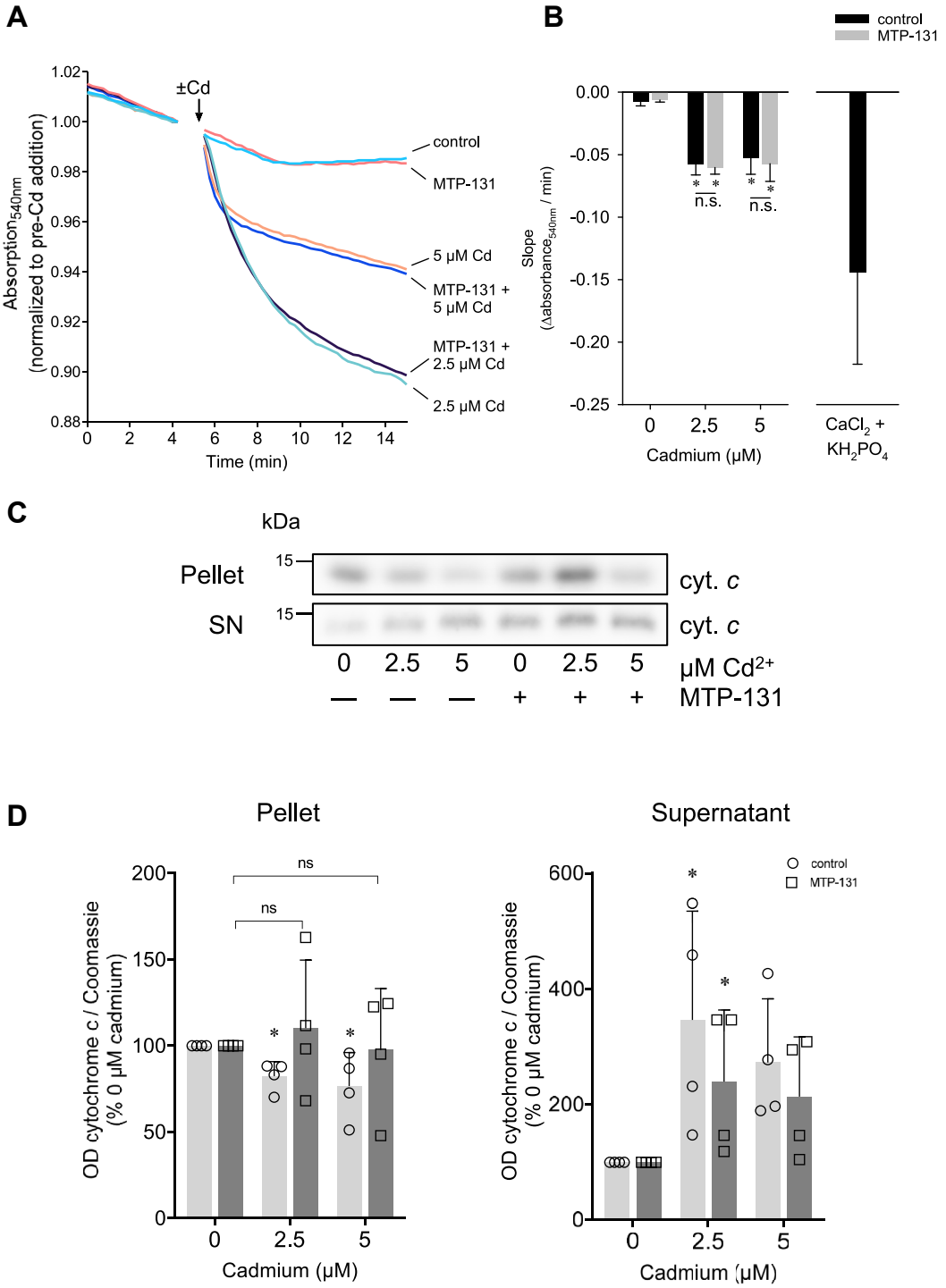

Fig. 5. MTP-131 does not prevent cadmium-induced swelling but suppresses cytochrome *c* release from isolated rat kidney cortex mitochondria. A: Crude rKC_{mito} suspended in iso-osmotic MSH buffer were energized with rotenone and succinate. When used, mitochondria were preincubated with 0.1 µM MTP-131 for 15 min at RT. Swelling was monitored by light scattering at λ_{540nm}. A representative experiment from n = 3–6 is shown. B: Slopes of swelling curves in (*A*) were determined from the first 45 s after Cd addition or the positive control of 0.1 mM $CaCl_2$ + 5 mM KH_2PO_4 (n = 3–6). C: Mitochondrial suspensions at the end of experiments in (A) were separated by centrifugation. Proteins from supernatants (SNs) were concentrated by trichloroacetic acid precipitation. Pellets and SNs were immunoblotted for cytochrome *c* (cyt. *c*) using Coomassie staining to control for loading. D: Densitometry analysis of cyt. *c* signals in mitochondrial pellet and SN showed Cd-induced cyt. *c* release from pellets was attenuated by MTP-131 (n = 4).

lipid-protein interactions. The pivotal function of CL in SC formation and stabilization has been well-described (30, 79) though other factors, such as non-SC proteins or lipid composition, may also contribute. CL seems to form the "glue" holding multiple ETC complexes together, thus the correct CL dosage and ratio of CL,

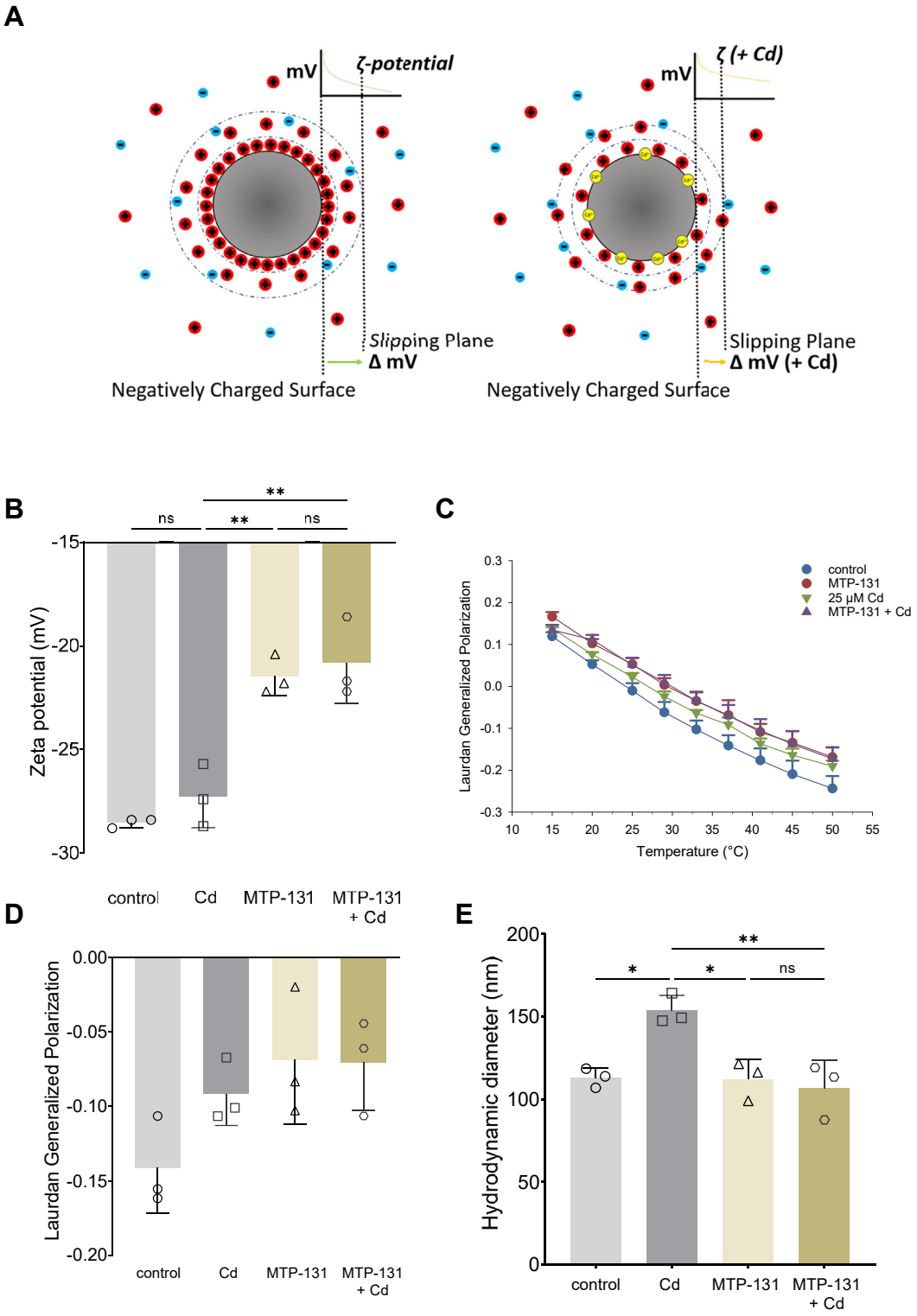

Fig. 6. MTP-131 hinders cadmium binding to IMM biomimetic nanoliposomes, Nanoliposomes were comprised of 40 mol % POPC, 35 mol % DOPE, 20 mol % TOCL, and 5 mol % SAPI to mimic the IMM. A: Diagram of zeta potential in the absence (left) and presence (right) of Cd. From 0.1 mM IMM biomimetic nanoliposomes suspended in 20 mM HEPES, 100 mM NaCl, pH 7.4, zeta potential (B), laurdan GP (C, D), and hydrodynamic diameter (E) was determined in the presence of Cd alone (25 μM; 5 min) or in co-incubation with MTP-131 (0.1 mM). Laurdan was added to nanoliposomes after treatment. Membrane MTP-131 binding reduces the net negative charge localized at the nanoliposome surface, therefore decreasing the electrochemical potential at the slipping plane through reduced charge accumulation (A, B). Data from technical triplicates from 3 independent nanoliposome preparations are shown.

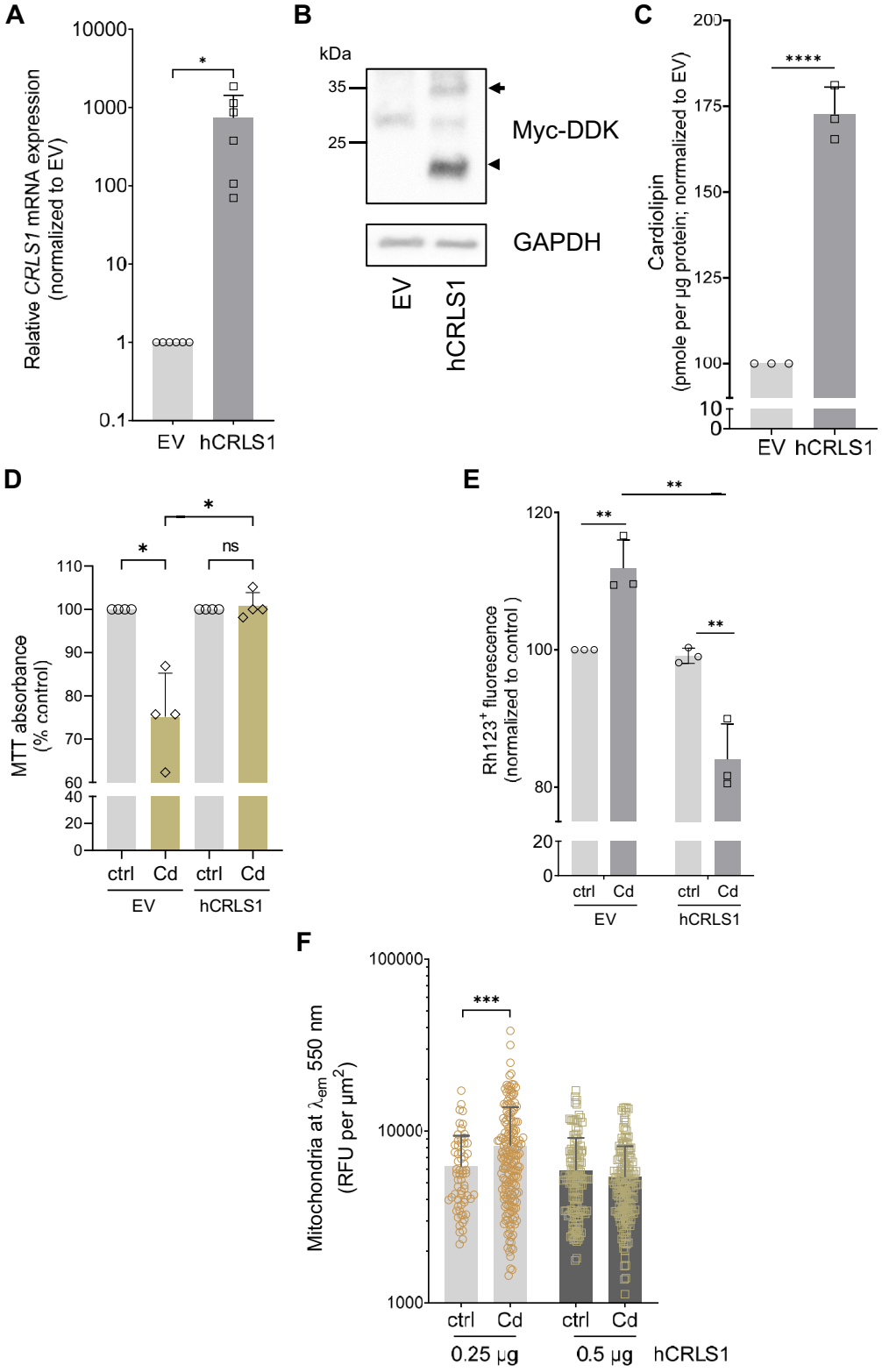

Fig. 7. Expression of cardiolipin synthase 1 (CRLS1) rescues cadmium cytotoxicity. A: *CRLS1* mRNA abundancy after transient transfection of HPCT cells for 24 h with 0.5 µg Myc-DDK-hCRLS1 plasmid or pCMV6-entry empty vector (EV) was assessed by qPCR (n = 6). B: Overexpression of Myc-DDK-tagged CRLS1 protein was confirmed by immunoblotting of whole-cell lysates with anti-DDK antibody. Transcript variants 1 (*arrow*) and 2 (*arrowhead*) are seen. Anti-GAPDH antibody signal was used as a loading control. C: Analysis of CL extracted from whole cell HPCT pellets (50–100 µg protein) by LC-MS/MS confirmed functional CRLS1 in Myc-DDK-hCRLS1 transfected cells (n = 3). D: Viability of hCRLS1-HPCT cells exposed to 5 µM Cd for 24 h was determined by MTT assay relative to transfected untreated controls (n = 4). E: reversal and reduction of ROS formation by 5 µM Cd for 3 h in hCRLS1-transfected HPCT cells measured by oxidation of DHR123 to Rh123^{+} at $\lambda_{ex}/\lambda_{em}$ 485/535 nm (n = 3) as compared to Cd-treated EV cells. F: HPCT cells were transiently transfected with 0.25 µg or 0.5 µg Myc-DDK-hCRLS1 plasmid for 24 h. After 1 µM Cd exposure for 1 h, cells were loaded with di-4-ANEPPDHQ and imaged at $\lambda_{ex}/\lambda_{em}$ 485/550 nm, which detects liquid-ordered domains. Fluorescence intensity from >50 selected regions of mitochondria were analyzed from 50 cells per condition and two independent experiments.

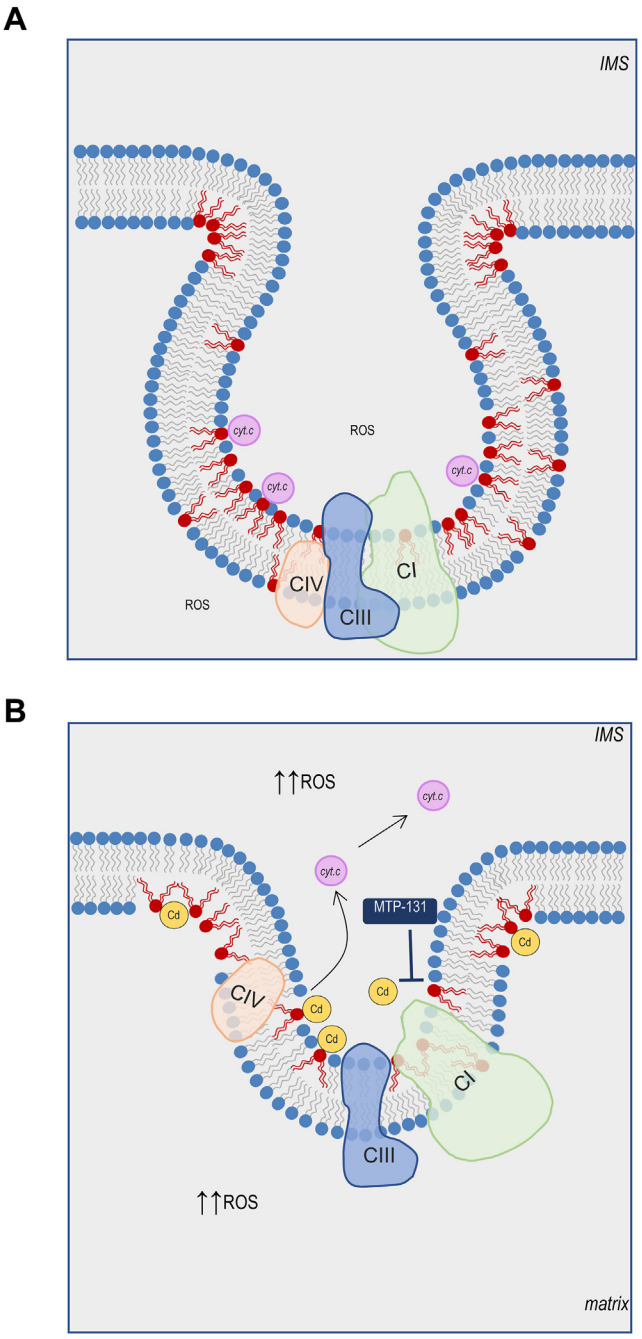

Fig. 8. Mitochondrial dysfunction mediated by Cd-CL interaction (model). A: In healthy mitochondria, negative membrane curvature and cristae formation mediated by the cone structure of CL (red lipids) supports SC assembly, which promotes efficient ATP synthesis and limits ROS release into the matrix and intermembrane space (IMS). A pool of cytochrome *c* (cyt. *c*) is associated with CL. B: Cd entry into mitochondria results in electrostatic interactions and binding with CL's two polar headgroups resulting in expansion of the hydrophobic tails, limitation of membrane curvature and lipid lateral diffusion, and culminates in membrane rigidification and disruption of SC formation. Consequently, ROS generation is increased, which creates oxidative stress. Additionally, Cd displaces cyt. *c* from CL and promotes its release into the cytosol where it induces apoptosis by the formation of the apoptosome, caspase activation, and protein cleavage. The CL aggregator drug MTP-131/elamipretide abolishes Cd-CL interactions and prevents Cd-induced ROS and cytotoxicity.

phospholipids, and transmembrane proteins are critical in maintaining efficient electron transfer whilst keeping ROS to a minimum (Fig. 8). Our experimental approach to maintain available CL with MTP-131 or CRLS1 effectively abolished Cd-induced IMM/CL rigidification and ROS (Figs. 3–8). Though CRLS1 is Mn^{2+}-dependent, endogenous CL levels were unchanged by Cd (1.03 vs. 1.04 pmol/μg protein, data not shown).

Based on studies with Ca^{2+}-CL (54, 80) and the highly similar ionic radii of Ca^{2+} and Cd^{2+} (81), it may be assumed that Cd acts like Ca^{2+}. Yet the inorganic chemistry of Cd and Ca^{2+} suggests that Cd may actually be more effective in CL-binding. Cd's relatively high electronegativity (Cd 1.69 vs. Ca^{2+} 1.0 (82)) combined with a low hydration enthalpy (Cd −1807 kJ/mol (83)) means a stronger association with negative CL moieties and less energy is required for desolvation. Dehydration energies and the differing complexation geometries between Cd (tetrahedral and octahedral) and Ca^{2+} (pentagonal bipyramidal) could be additional contributing factors. Based on an estimated electrolyte composition of the IMS (120 mM K^+, 14.5 mM Na^+, 4 mM Cl^-, 1 mM Mg^{2+}, 0.1 μM Ca^{2+}, pH 6.9), Cd speciates into 86.8% Cd^{2+}, 13.0% $CdCl^+$, 0.03% $CdOH^+$, and 0.1% $CdCl_2$[1]. Hence, the divalent Cd^{2+} ion mostly likely forces proximity of two CL phosphate headgroups (Fig. 2H), expanding space between adjacent phospholipid polar groups (explaining decreased laurdan GP in mitoplasts) as well as between hydrophobic tails, decreasing lateral diffusion of IMM phospholipids, resulting in hydrophobic core stiffness (12) (Figs. 1, 2, 6, and 8B), and potentiating diminished negative curvature and/or lamellar-to-hexagonal phase transition (54, 69). Alternatively, Cd^{2+} could bind to the phosphate headgroups of adjacent CL molecules with the same outcome as detailed above (Fig. 8B).

CL lipid chemistry is important in mitochondrial processes. Ca^{2+} increases the susceptibility of CL oxidation (80), which is a prerequisite for cytochrome *c* liberation (84). Thus, cytochrome *c* release by Cd (23) (Fig. 5C, D) may be exacerbated by Cd-induced ROS in a self-propagating cycle (32). Intriguingly, ROS generation seems not be responsible for Cd-induced SC disruption (Figs. 3D, E, supplemental Fig. S4). Additionally, dissipation of the mitochondrial pH gradient by Cd (25) promotes the dianion-CL species, which causes membrane stiffness and flattening (68), and would favor cationic interactions, such as with Cd.

MTP-131/elamipretide has successfully treated clinical trial patients with mitochondrial defects, such as Barth syndrome, where *TAZ* gene mutations disrupt phospholipid – including CL – synthesis (85). Indeed, the U.S. Food and Drug Administration (FDA) have

[1]Predicted by chemical equilibrium software Visual MINTEQ (https://vminteq.com/).

very recently accepted a new drug application for MTP-131/elamipretide for the treatment of Barth syndrome[2], making it the first approved therapy for the debilitating disease should it be approved. Intriguingly, symptoms associated with diabetic nephropathy (86), glomerulopathy (87), renal ischemic injury (58, 88), and mitochondrial-driven inflammation in aged kidney (89) can be alleviated by the investigational drug. Since chronic exposures of toxic metals, such as Cd, Pb, As, and Cr, culminate in accumulation in tubular cells of the kidney, the protective effect of MTP-131 against Cd-induced mitochondrial damage could potentially represent a new therapeutic opportunity for the alleviation and/or prevention of metal nephrotoxicity.

Data availability

The authors confirm that the data supporting the findings of this study are available within the article and its supplementary materials.

Supplemental data

This article contains supplemental data.

Acknowledgments

We like to thank Drs. Craig Brideau and Pina Colarusso (Live Cell Imaging Laboratory, Snyder Institute for Chronic Diseases, Cummings School of Medicine, University of Calgary) for assistance with live multiphoton and confocal scanning microscopy as well as Michelle Maaß (Witten/Herdecke University) for expert technical assistance.

Author contributions

E. J. P., W. K. L., F. T., T. I., and N. R. writing–review & editing; E. J. P., W. K. L., F. T., T. I., D. H., and N. R. writing–original draft; E. J. P., W. K. L., T. I., D. H., and N. R. visualization; E. J. P. and W. K. L. supervision; E. J. P., W. K. L., and F. T. resources; E. J. P., W. K. L., F. T., T. I., and K. S. funding acquisition; E. J. P., W. K. L., and F. T. conceptualization. W. K. L. project administration; W. K. L. and N. R. methodology, W. K. L., M. P., T. I., D. H., N. R., and K. S. investigation; W. K. L., M. P., T. I., D. H., N. R., and K. S. formal analysis.

Author ORCIDs

Nadiya Romanova https://orcid.org/0000-0002-5505-3279
Kevin Sule https://orcid.org/0000-0003-3881-8951
Travis Issler https://orcid.org/0009-0004-3426-7341
Frank Thévenod https://orcid.org/0000-0001-8663-3498
Elmar J. Prenner https://orcid.org/0000-0002-4821-2657
Wing-Kee Lee https://orcid.org/0000-0002-7352-4679

[2]Press release April 8 2024 Stealth Biotherapeutics. (https://stealthbt.com/stealth-biotherapeutics-announces-fda-acceptance-of-new-drug-application-for-elamipretide-for-the-treatment-of-barth-syndrome/).

Funding and additional information

Funding was received from the German Research Foundation (Deutsche Forschungsgemeinschaft; LE2387 8-1 and LE2387 9-1 to W. K. L.). T. I. and K. S. were supported by Mitacs Globalink Research Awards. E. J. P was supported by an NSERC Discovery grant (RGPIN-2024-03950).

Conflict of interest

The authors declare that they have no conflicts of interest with the contents of this article.

Abbreviations

CI, complex I; CIII, complex III; CIV, complex IV; Cd, cadmium; CL, cardiolipin; CRLS1, cardiolipin synthase 1; cyt *c*, cytochrome *c*; DHR123, dihydrorhodamine 123; DMT1, divalent metal transporter 1; DOPE, dioleoylphosphatidylethanolamine; DPH, diphenylhexatriene; ETC, electron transport chain; EV, empty vector; FDA, U.S. Food and Drug Administration; GP, generalized polarization; GSH, glutathione (reduced); HPCT, human proximal convoluted tubule; IB, immunoblot; IMM, inner mitochondrial membrane; IMS, intermembrane space; LUV, large unilamellar vesicle; MCU, mitochondrial calcium uniporter; MLV, multilamellar vesicle; MT, metallothionein; MTT, 3-(4,5-Dimethylthiazol-2-yl)-2,5-diphenyltetrazolium bromide; OML, outer membrane leaflet; OMM, outer mitochondrial membrane; PC, phosphatidylcholine; PE, phosphatidylethanolamine; PM, plasma membrane; $Rh123^{+}$, rhodamine 123^{+}; rKC_{mito}, rat kidney cortex mitochondria; ROS, reactive oxygen species; SAPI, stearoyl-arachidonoyl-phosphatidylinositol; SC, supercomplex; SFM, serum free medium; TLCL, tetralinoleoyl cardiolipin; TMCL, tetramyristoyl cardiolipin; TOCL, tetraoleoyl cardiolipin; VDAC, voltage dependent anion channel.

Manuscript received August 29, 2024, and in revised form January 21, 2025. Published, JLR Papers in Press, January 27, 2025, https://doi.org/10.1016/j.jlr.2025.100750

REFERENCES

1. Fels, J., Scharner, B., Zarbock, R., Zavala Guevara, I. P., Lee, W. K., Barbier, O. C., *et al.* (2019) Cadmium complexed with beta2-Microglubulin, albumin and lipocalin-2 rather than metallothionein cause Megalin:Cubilin dependent toxicity of the renal proximal tubule. *Int. J. Mol. Sci.* **20**, 2379
2. Freisinger, E., and Vasak, M. (2013) Cadmium in metallothioneins. *Met. Ions Life Sci.* **11**, 339–371
3. Mah, V., and Jalilehvand, F. (2010) Cadmium(II) complex formation with glutathione. *J. Biol. Inorg. Chem.* **15**, 441–458
4. Thévenod, F., and Lee, W. K. (2013) Toxicology of cadmium and its damage to mammalian organs. *Met. Ions Life Sci.* **11**, 415–490
5. Martinez-Finley, E. J., Chakraborty, S., Fretham, S. J., and Aschner, M. (2012) Cellular transport and homeostasis of essential and nonessential metals. *Metallomics.* **4**, 593–605
6. Satarug, S., Vesey, D. A., Gobe, G. C., and Phelps, K. R. (2024) The pathogenesis of albuminuria in cadmium nephropathy. *Curr. Res. Toxicol.* **6**, 100140
7. Doccioli, C., Sera, F., Francavilla, A., Cupisti, A., and Biggeri, A. (2024) Association of cadmium environmental exposure with chronic kidney disease: a systematic review and meta-analysis. *Sci. Total Environ.* **906**, 167165
8. Hassanin, M., Kerek, E., Chiu, M., Anikovskiy, M., and Prenner, E. J. (2016) Binding affinity of inorganic mercury and cadmium to biomimetic erythrocyte membranes. *J. Phys. Chem. B.* **120**, 12872–12882

9. Stubbs, C. D. (1983) Membrane fluidity: structure and dynamics of membrane lipids. *Essays Biochem.* **19**, 1–39
10. Kerek, E., Hassanin, M., and Prenner, E. J. (2018) Inorganic mercury and cadmium induce rigidity in eukaryotic lipid extracts while mercury also ruptures red blood cells. *Biochim. Biophys. Acta Biomembr.* **1860**, 710–717
11. Sovago, I., and Varnagy, K. (2013) Cadmium(II) complexes of amino acids and peptides. *Met. Ions Life Sci.* **11**, 275–302
12. Kerek, E. M., and Prenner, E. J. (2016) Inorganic cadmium affects the fluidity and size of phospholipid based liposomes. *Biochim. Biophys. Acta.* **1858**, 3169–3181
13. Bae, Y. S., Oh, H., Rhee, S. G., and Yoo, Y. D. (2011) Regulation of reactive oxygen species generation in cell signaling. *Mol. Cells.* **32**, 491–509
14. Sies, H., and Jones, D. P. (2020) Reactive oxygen species (ROS) as pleiotropic physiological signalling agents. *Nat. Rev. Mol. Cell Biol.* **21**, 363–383
15. Mitchell, P. (1961) Coupling of phosphorylation to electron and hydrogen transfer by a chemi-osmotic type of mechanism. *Naturwissenschaften.* **191**, 144–148
16. Letts, J. A., Fiedorczuk, K., and Sazanov, L. A. (2016) The architecture of respiratory supercomplexes. *Nature.* **537**, 644–648
17. Lopez-Fabuel, I., Le Douce, J., Logan, A., James, A. M., Bonvento, G., Murphy, M. P., *et al.* (2016) Complex I assembly into supercomplexes determines differential mitochondrial ROS production in neurons and astrocytes. *Proc. Natl. Acad. Sci. U. S. A.* **113**, 13063–13068
18. Maranzana, E., Barbero, G., Falasca, A. I., Lenaz, G., and Genova, M. L. (2013) Mitochondrial respiratory supercomplex association limits production of reactive oxygen species from complex I. *Antioxid. Redox Signal.* **19**, 1469–1480
19. Waku, K. (1984) The chemical form of cadmium in subcellular fractions following cadmium exposure. *Environ. Health Perspect.* **54**, 37–44
20. Szabo, I., and Szewczyk, A. (2023) Mitochondrial ion channels. *Annu. Rev. Biophys.* **52**, 229–254
21. Reina, S., Pittala, M. G. G., Guarino, F., Messina, A., De Pinto, V., Foti, S., *et al.* (2020) Cysteine oxidations in mitochondrial membrane proteins: the case of VDAC isoforms in mammals. *Front. Cell Dev. Biol.* **8**, 397
22. Gray, H. B., and Winkler, J. R. (2003) Electron tunneling through proteins. *Q. Rev. Biophys.* **36**, 341–372
23. Lee, W. K., Bork, U., Gholamrezaei, F., and Thévenod, F. (2005) Cd(2+)-induced cytochrome c release in apoptotic proximal tubule cells: role of mitochondrial permeability transition pore and Ca(2+) uniporter. *Am. J. Physiol. Ren. Physiol.* **288**, F27–F39
24. Ying, W. L., Emerson, J., Clarke, M. J., and Sanadi, D. R. (1991) Inhibition of mitochondrial calcium ion transport by an oxo-bridged dinuclear ruthenium ammine complex. *Biochemistry.* **30**, 4949–4952
25. Lee, W. K., Spielmann, M., Bork, U., and Thévenod, F. (2005) Cd^{2+}-induced swelling-contraction dynamics in isolated kidney cortex mitochondria: role of Ca^{2+} uniporter, K^+ cycling, and protonmotive force. *Am. J. Physiol. Cell Physiol.* **289**, C656–C664
26. Korotkov, S. M., Skulskii, I. A., and Glazunov, V. V. (1998) Cd^{2+} effects on respiration and swelling of rat liver mitochondria were modified by monovalent cations. *J. Inorg. Biochem.* **70**, 17–23
27. Wang, Y., Fang, J., Leonard, S. S., and Rao, K. M. (2004) Cadmium inhibits the electron transfer chain and induces reactive oxygen species. *Free Radic. Biol. Med.* **36**, 1434–1443
28. Kondoh, M., Ogasawara, S., Araragi, S., Higashimoto, M., and Sato, M. (2001) Cytochrome c release from mitochondria induced by cadmium. *J. Health Sci.* **47**, 78–82
29. Pfeiffer, K., Gohil, V., Stuart, R. A., Hunte, C., Brandt, U., Greenberg, M. L., *et al.* (2003) Cardiolipin stabilizes respiratory chain supercomplexes. *J. Biol. Chem.* **278**, 52873–52880
30. Arnarez, C., Marrink, S. J., and Periole, X. (2016) Molecular mechanism of cardiolipin-mediated assembly of respiratory chain supercomplexes. *Chem. Sci.* **7**, 4435–4443
31. Ikon, N., and Ryan, R. O. (2017) Cardiolipin and mitochondrial cristae organization. *Biochim. Biophys. Acta Biomembr.* **1859**, 1156–1163
32. Lee, W. K., Probst, S., Scharner, B., Deba, T., Dahdouh, F., and Thévenod, F. (2024) Distinct concentration-dependent oxidative stress profiles by cadmium in a rat kidney proximal tubule cell line. *Arch. Toxicol.* **98**, 1043–1059
33. Casalino, E., Calzaretti, G., Sblano, C., and Landriscina, C. (2002) Molecular inhibitory mechanisms of antioxidant enzymes in rat liver and kidney by cadmium. *Toxicology.* **179**, 37–50
34. Orosz, D. E., Woost, P. G., Kolb, R. J., Finesilver, M. B., Jin, W., Frisa, P. S., *et al.* (2004) Growth, immortalization, and differentiation potential of normal adult human proximal tubule cells. *In Vitro Cell Dev. Biol. Anim.* **40**, 22–34
35. Langelueddecke, C., Roussa, E., Fenton, R. A., Wolff, N. A., Lee, W. K., and Thévenod, F. (2012) Lipocalin-2 (24p3/neutrophil gelatinase-associated lipocalin (NGAL)) receptor is expressed in distal nephron and mediates protein endocytosis. *J. Biol. Chem.* **287**, 159–169
36. Lee, W. K., Probst, S., Santoyo-Sanchez, M. P., Al-Hamdani, W., Diebels, I., von Sivers, J. K., *et al.* (2017) Initial autophagic protection switches to disruption of autophagic flux by lysosomal instability during cadmium stress accrual in renal NRK-52E cells. *Arch. Toxicol.* **91**, 3225–3245
37. Parasassi, T., Krasnowska, E. K., Bagatolli, L., and Gratton, E. (1998) LAURDAN and PRODAN as polarity-sensitive fluorescent membrane probes. *J. Fluoresc.* **8**, 365–373
38. Kaiser, R. D., and London, E. (1998) Location of diphenylhexatriene (DPH) and its derivatives within membranes: comparison of different fluorescence quenching analyses of membrane depth. *Biochemistry.* **37**, 8180–8190
39. He, W. (2023) DPH probe method for liposome-membrane fluidity determination. *Methods Mol. Biol.* **2622**, 241–244
40. Schindelin, J., Arganda-Carreras, I., Frise, E., Kaynig, V., Longair, M., Pietzsch, T., *et al.* (2012) Fiji: an open-source platform for biological-image analysis. *Nat. Methods.* **9**, 676–682
41. Greenawalt, J. W. (1974) The isolation of outer and inner mitochondrial membranes. *Methods Enzymol.* **31**, 310–323
42. Timon-Gomez, A., Perez-Perez, R., Nyvltova, E., Ugalde, C., Fontanesi, F., and Barrientos, A. (2020) Protocol for the analysis of yeast and human mitochondrial respiratory chain complexes and supercomplexes by blue native electrophoresis. *STAR Protoc.* **1**, 100089
43. Schagger, H., and von Jagow, G. (1991) Blue native electrophoresis for isolation of membrane protein complexes in enzymatically active form. *Anal. Biochem.* **199**, 223–231
44. Denizot, F., and Lang, R. (1986) Rapid colorimetric assay for cell growth and survival. Modifications to the tetrazolium dye procedure giving improved sensitivity and reliability. *J. Immunol. Methods.* **89**, 271–277
45. Daum, G. (1985) Lipids of mitochondria. *Biochim. Biophys. Acta.* **822**, 1–42
46. Ames, B. N. (1966) Assay of inorganic phosphate, total phosphate and phosphatases. In *Complex Carbohydrates.* E. F. Neufeld and V. Ginsburg, editors, 115–118
47. Wang, D. Y., van der Mei, H. C., Ren, Y., Busscher, H. J., and Shi, L. (2019) Lipid-based antimicrobial delivery-systems for the treatment of bacterial infections. *Front. Chem.* **7**, 872
48. Marquardt, D., Geier, B., and Pabst, G. (2015) Asymmetric lipid membranes: towards more realistic model systems. *Membranes (Basel).* **5**, 180–196
49. Daear, W., Mundle, R., Sule, K., and Prenner, E. J. (2021) The degree and position of phosphorylation determine the impact of toxic and trace metals on phosphoinositide containing model membranes. *BBA Adv.* **1**, 100021
50. Folch, J., Lees, M., and Sloane Stanley, G. H. (1957) A simple method for the isolation and purification of total lipides from animal tissues. *J. Biol. Chem.* **226**, 497–509
51. Xu, G., Liu, X., Shu, Y., Pillai, J. A., and Xu, Y. (2018) A rapid and sensitive LC-MS/MS method for quantitative analysis of cardiolipin (18:2)(4) in human leukocytes and mouse skeletal muscles. *J. Pharm. Biomed. Anal.* **158**, 386–394
52. Kucherak, O. A., Oncul, S., Darwich, Z., Yushchenko, D. A., Arntz, Y., Didier, P., *et al.* (2010) Switchable nile red-based probe for cholesterol and lipid order at the outer leaflet of biomembranes. *J. Am. Chem. Soc.* **132**, 4907–4916
53. Korchowiec, B., Janikowska-Sagan, M., Kwiecinska, K., Stachowicz-Kusnierz, A., and Korchowiec, J. (2021) The role of cholesterol in membrane activity of digitonin: experimental and theoretical model studies. *J. Mol. Liq.* **323**, 114598
54. Fox, C. A., Ellison, P., Ikon, N., and Ryan, R. O. (2019) Calcium-induced transformation of cardiolipin nanodisks. *Biochim. Biophys. Acta Biomembr.* **1861**, 1030–1036

55. Issler, T., Sule, K., Lewrenz, A. M., and Prenner, E. J. (2024) Differential interactions of essential and toxic metal ions with biologically relevant phosphatidic acid and phosphatidylserine membranes. *Biometals.* **37**, 631–648
56. Levental, I., and Lyman, E. (2023) Regulation of membrane protein structure and function by their lipid nano-environment. *Nat. Rev. Mol. Cell Biol.* **24**, 107–122
57. Zhao, K., Zhao, G. M., Wu, D., Soong, Y., Birk, A. V., Schiller, P. W., *et al.* (2004) Cell-permeable peptide antioxidants targeted to inner mitochondrial membrane inhibit mitochondrial swelling, oxidative cell death, and reperfusion injury. *J. Biol. Chem.* **279**, 34682–34690
58. Birk, A. V., Liu, S., Soong, Y., Mills, W., Singh, P., Warren, J. D., *et al.* (2013) The mitochondrial-targeted compound SS-31 re-energizes ischemic mitochondria by interacting with cardiolipin. *J. Am. Soc. Nephrol.* **24**, 1250–1261
59. Mitchell, W., Ng, E. A., Tamucci, J. D., Boyd, K. J., Sathappa, M., Coscia, A., *et al.* (2020) The mitochondria-targeted peptide SS-31 binds lipid bilayers and modulates surface electrostatics as a key component of its mechanism of action. *J. Biol. Chem.* **295**, 7452–7469
60. Fox, C. A., and Ryan, R. O. (2022) Studies of the cardiolipin interactome. *Prog. lipid Res.* **88**, 101195
61. Lee, W. K., Thevenod, F., and Prenner, E. J. (2024) Global threat posed by metals and metalloids in the changing environment: a One Health approach to mechanisms of toxicity. *Biometals.* **37**, 539–544
62. European, Food, Safety, and Authority. (2012) Cadmium dietary exposure in the European population. *EFSA J.* **10**, 2551
63. Branca, J. J. V., Pacini, A., Gulisano, M., Taddei, N., Fiorillo, C., and Becatti, M. (2020) Cadmium-induced cytotoxicity: effects on mitochondrial electron transport chain. *Front. Cell Dev. Biol.* **8**, 604377
64. Le, C. T. M., Houri, A., Balage, N., Smith, B. J., and Mechler, A. (2019) Interaction of small ionic species with phospholipid membranes: the role of metal coordination. *Front. Mater.* **5**, 80
65. Sule, K., Umbsaar, J., and Prenner, E. J. (2020) Mechanisms of Co, Ni, and Mn toxicity: from exposure and homeostasis to their interactions with and impact on lipids and biomembranes. *Biochim. Biophys. Acta Biomembr.* **1862**, 183250
66. Baker, N., Patel, J., and Khacho, M. (2019) Linking mitochondrial dynamics, cristae remodeling and supercomplex formation: how mitochondrial structure can regulate bioenergetics. *Mitochondrion.* **49**, 259–268
67. Stephan, T., Bruser, C., Deckers, M., Steyer, A. M., Balzarotti, F., Barbot, M., *et al.* (2020) MICOS assembly controls mitochondrial inner membrane remodeling and crista junction redistribution to mediate cristae formation. *EMBO J.* **39**, e104105
68. Venkatraman, K., Lee, C. T., Garcia, G. C., Mahapatra, A., Milshteyn, D., Perkins, G., *et al.* (2023) Cristae formation is a mechanical buckling event controlled by the inner mitochondrial membrane lipidome. *EMBO J.* **42**, e114054
69. Ortiz, A., Killian, J. A., Verkleij, A. J., and Wilschut, J. (1999) Membrane fusion and the lamellar-to-inverted-hexagonal phase transition in cardiolipin vesicle systems induced by divalent cations. *Biophys. J.* **77**, 2003–2014
70. Muller, M. P., Jiang, T., Sun, C., Lihan, M., Pant, S., Mahinthichaichan, P., *et al.* (2019) Characterization of lipid-protein interactions and lipid-mediated modulation of membrane protein function through molecular simulation. *Chem. Rev.* **119**, 6086–6161
71. Killian, J. A., Koorengevel, M. C., Bouwstra, J. A., Gooris, G., Dowhan, W., and de Kruijff, B. (1994) Effect of divalent cations on lipid organization of cardiolipin isolated from Escherichia coli strain AH930. *Biochim. Biophys. Acta.* **1189**, 225–232
72. Rietveld, A. G., Killian, J. A., Dowhan, W., and de Kruijff, B. (1993) Polymorphic regulation of membrane phospholipid composition in Escherichia coli. *J. Biol. Chem.* **268**, 12427–12433
73. Wolff, N. A., Ghio, A. J., Garrick, L. M., Garrick, M. D., Zhao, L., Fenton, R. A., *et al.* (2014) Evidence for mitochondrial localization of divalent metal transporter 1 (DMT1). *FASEB J.* **28**, 2134–2145
74. Pennington, E. R., Funai, K., Brown, D. A., and Shaikh, S. R. (2019) The role of cardiolipin concentration and acyl chain composition on mitochondrial inner membrane molecular organization and function. *Biochim. Biophys. Acta Mol. Cell Biol. Lipids.* **1864**, 1039–1052
75. Unsay, J. D., Cosentino, K., Subburaj, Y., and Garcia-Saez, A. J. (2013) Cardiolipin effects on membrane structure and dynamics. *Langmuir.* **29**, 15878–15887
76. Toury, R., Boissonneau, E., Stelly, N., Dupuis, Y., Berville, A., and Perasso, R. (1985) Mitochondria alterations in Cd^{2+}-treated rats: general regression of inner membrane cristae and electron transport impairment. *Biol. Cell.* **55**, 71–85
77. Vercellino, I., and Sazanov, L. A. (2022) The assembly, regulation and function of the mitochondrial respiratory chain. *Nat. Rev. Mol. Cell Biol.* **23**, 141–161
78. Chaban, Y., Boekema, E. J., and Dudkina, N. V. (2014) Structures of mitochondrial oxidative phosphorylation supercomplexes and mechanisms for their stabilisation. *Biochim. Biophys. Acta.* **1837**, 418–426
79. Zhang, M., Mileykovskaya, E., and Dowhan, W. (2005) Cardiolipin is essential for organization of complexes III and IV into a supercomplex in intact yeast mitochondria. *J. Biol. Chem.* **280**, 29403–29408
80. Miranda, E. G. A., Araujo-Chaves, J. C., Kawai, C., Brito, A. M. M., Dias, I. W. R., Arantes, J. T., *et al.* (2019) Cardiolipin structure and oxidation are affected by Ca(2+) at the interface of lipid bilayers. *Front. Chem.* **7**, 930
81. Marcus, Y. (1988) Ionic radii in aqueous solutions. *Chem. Rev.* **88**, 1475–1498
82. Allred, A. L. (1961) Electronegativity values from thermochemical data. *J. Inorg. Nucl. Chem.* **17**, 215–221
83. Smith, D. W. (1977) Ionic hydration enthalpies. *J. Chem. Educ.* **54**, 540–542
84. Petrosillo, G., Ruggiero, F. M., and Paradies, G. (2003) Role of reactive oxygen species and cardiolipin in the release of cytochrome c from mitochondria. *FASEB J.* **17**, 2202–2208
85. Thompson, W. R., Manuel, R., Abbruscato, A., Carr, J., Campbell, J., Hornby, B., *et al.* (2024) Long-term efficacy and safety of elamipretide in patients with barth syndrome: 168-week open-label extension results of TAZPOWER. *Genet. Med.* **26**, 101138
86. Miyamoto, S., Zhang, G., Hall, D., Oates, P. J., Maity, S., Madesh, M., *et al.* (2020) Restoring mitochondrial superoxide levels with elamipretide (MTP-131) protects db/db mice against progression of diabetic kidney disease. *J. Biol. Chem.* **295**, 7249–7260
87. Szeto, H. H., Liu, S., Soong, Y., Alam, N., Prusky, G. T., and Seshan, S. V. (2016) Protection of mitochondria prevents high-fat diet-induced glomerulopathy and proximal tubular injury. *Kidney Int.* **90**, 997–1011
88. Saad, A., Herrmann, S. M. S., Eirin, A., Ferguson, C. M., Glockner, J. F., Bjarnason, H., *et al.* (2017) Phase 2a clinical trial of mitochondrial protection (elamipretide) during stent revascularization in patients with atherosclerotic renal artery stenosis. *Circ. Cardiovasc. Interv.* **10**, e005487
89. [preprint] Saleh, T. A., Whitson, J. A., Keiser, P., Prasad, P., Jenkins, B. C., Sodeinde, T., *et al.* (2024) Metabolite accumulation from oral NMN supplementation drives aging-specific kidney inflammation. *bioRxiv.* https://doi.org/10.1101/2024.04.09.588624